國立臺灣大學理學院物理學研究所

博士論文

Department of Physics

College of Science

National Taiwan University

Doctoral Dissertation

輻射力矩對塵埃的破壞及對日光層塵埃尺寸演變的影響的研究

Investigating the influence of the radiative torque disruption on the size evolution of dust in the heliosphere

吳志恆

Chi-Hang Ng

指導教授: 薛熙于 博士

共同指導老師: 辜品高 博士

Advisor: Hsi-Yu Schive Ph.D.

Co-advisor: Pin-Gao Gu Ph.D.

中華民國 114 年 7 月

July, 2025

國立臺灣大學博士學位論文
口試委員會審定書
PhD DISSERTATION ACCEPTANCE CERTIFICATE
NATIONAL TAIWAN UNIVERSITY

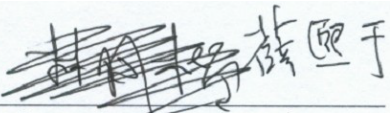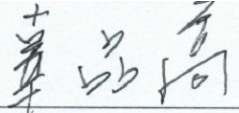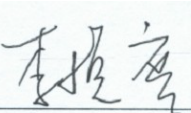（論文中文題目）(Chinese title of PhD dissertation)

輻射力矩對塵埃的破壞及對日光層塵埃尺寸演變的影響的研究

（論文英文題目）(English title of PhD dissertation)

Investigating the Influence of Radiative Torque Disruption on the Size Evolution of Dust in the Heliosphere

本論文係＿＿吳志恆＿＿(姓名)＿D04222001＿（學號）在國立臺灣大學＿物理系物理所＿(系/所/學位學程)完成之博士學位論文，於民國 114 年 07 月 08 日承下列考試委員審查通過及口試及格，特此證明。

The undersigned, appointed by the Department / Institute of ＿＿＿Physics＿＿＿

on ＿08＿(date)＿07＿(month)＿2025＿(year) have examined a PhD dissertation entitled above presented by＿＿Chi-Hang Ng＿＿(name)＿＿D04222001＿＿(student ID) candidate and hereby certify that it is worthy of acceptance.

口試委員 Oral examination committee：

（指導教授 Advisor）

摘要

本論文探討了輻射扭矩破壞（Radiative Torque Disruption, RATD）機制在太陽系內將微米級塵埃顆粒破碎成奈米顆粒過程中的作用。通過分析在不同離心力應力下的破壞時間尺度，我們證明 RATD 是一種高效分解微米級顆粒的過程，其效果超越其他破碎機制。此外，RATD 抑制了輻射壓力對微米級顆粒的驅逐，改變了它們在太陽系內的動力學行為。

研究揭示 RATD 顯著改變水雪線（water snow line）位置，使其超越熱力學定義的邊界，突顯溫度與顆粒尺寸對日球層動力學的雙重影響。對於較小的顆粒，由於 RATD 的影響，雪線可以延伸到其熱力學定義位置之外。此外，我們建立了一個簡化模型來描述由 RATD 修改後的顆粒大小分佈，揭示了微米級顆粒數密度的顯著減少以及次微米級顆粒數量的相應增加。然而研究顯示，若少於 80% 塵埃顆粒通過輻射扭矩作用於高 J 吸引子（high-J attractors）達到定向排列，RATD 對顆粒尺寸分布的影響將顯著減弱。

最後，我們提出了測試 RATD 機制的實驗方法，並討論了將我們的模型應用於太陽系塵埃研究時的不確定性。

關鍵字：塵埃、消光──星際介質：演化──星際介質：一般情況──太陽風

Abstract

This thesis investigates the role of the Radiative Torque Disruption (RATD) mechanism in the fragmentation of micrometer-sized dust grains into nanoparticles within the heliosphere. By analyzing the disruption timescales under varying centrifugal stresses, we demonstrate that RATD is an efficient process for breaking down micrometer-sized grains, surpassing other fragmentation mechanisms in its effectiveness. Additionally, RATD inhibits the expulsion of micrometer-sized grains by radiation pressure, altering their dynamical behavior within the heliosphere.

This study reveals that RATD significantly alters the water snow line's position beyond its thermally defined boundary, emphasizing the dual influence of temperature and grain size on heliospheric dynamics. For smaller grains, the snow line can extend beyond its thermally defined position due to the impact of RATD. Furthermore, we construct a simplified model to characterize the grain size distribution modified by RATD, revealing a substantial reduction in the number density

of micrometer-sized grains and a corresponding increase in sub-micrometer-sized grains. However, we find that if fewer than 80% of dust grains are aligned at high-J attractors by radiative torques, the impact of RATD on the grain size distribution is significantly weakened.
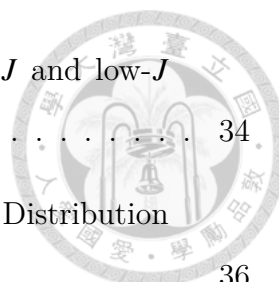
Finally, we propose experimental approaches to test the RATD mechanism and discuss the uncertainties associated with applying our model to heliospheric dust studies.

Keywords: dust, extinction – ISM: evolution – ISM: general – solar wind

Contents

List of Figures

Chapter 1   Introduction

The majority of the content in this thesis is based on Ng et al. (2025).

Remote sensing and in situ measurements within the heliosphere have revealed the presence of very small dust grains (radius below tens of nanometers, hereafter nanoparticles) that can be produced through various fragmentation mechanisms. The first in situ detection of micrometer-sized dust (radius between $0.1\,\mu\text{m}$ and $1000\,\mu\text{m}$) dates back to the Voyager missions, which observed dust around Saturn, Uranus, and Neptune (O'Shea et al., 2017). During the Voyager 2 mission, the planetary radio astronomy experiment detected intense unpolarized broadband noise, likely resulting from dust impacts on the spacecraft (Pedersen et al., 1991). Later missions, including Ulysses and Cassini, provided further evidence of dust particles in the heliosphere (e.g., Mann, 2017). Ulysses carried an in situ dust detector, enabling the direct observation of interstellar dust (ISD), interplanetary dust particles (IDP), and circumplanetary dust (e.g., Hsu et al., 2018; Jorgensen et al., 2021; Sterken et al., 2019). The Cassini spacecraft detected dust impacts around Saturn using both antennas (Ye et al., 2016) and a dedicated dust instrument (Kempf, 2008). Observations from Cassini's flyby around Jupiter confirmed that some dust streams originated from the volcanically active Jovian moon Io (Postberg et al., 2006). Data from Cassini suggested that nanoparticles are produced in the inner-

most heliosphere and are subsequently picked up by the solar wind (Schippers et al., 2015). Additional evidence for dust impact signals was found in measurements from the S/WAVES plasma wave antenna instruments on the STEREO spacecraft (O'Shea et al., 2017), with high nanoparticle velocities proposed to explain the frequency of detected events (Meyer-Vernet et al., 2009). These high velocities may be explained by the acceleration of charged particles by the solar wind (Czechowski & Mann, 2010). Furthermore, nanodust from comet 67P/Churyumov-Gerasimenko has been collected and analyzed by the MIDAS (Micro Imaging Dust Analysis System) (Mannel et al., 2019) and the IES (Ion and Electron Sensor) onboard the Rosetta spacecraft (LLera et al., 2020).

Remote observations have also highlighted the ubiquity of nanoparticles in debris disks. Near-infrared (NIR) observations have revealed excess emission from the inner regions of these disks, potentially near the silica sublimation zone (Ciardi et al., 2001). Defrère et al. (2011) detected hot dust in Vega, while Su et al. (2013) observed $2\,\mu$m emission excess in nearby debris disks around Vega and Fomalhaut, suggesting that nanoparticles with sizes of $5 - 20\,\text{nm}$ must be present within tens of stellar radii to explain these observations. van Lieshout et al. (2014) proposed that nanoparticles could originate from the collisional fragmentation of cometary dust grains (see also Lebreton et al., 2013). Spectroscopic observations by Bhowmik et al. (2019) further indicated the presence of very small grains in the debris disk around HD 32297, while submicron-sized silica grains were identified in the disks around HD 113766 and HD 172555 (Su et al., 2020). Various studies have suggested that nanoparticles can form through sublimation and collisional fragmentation (Mann, 2017; Mann et al., 2007; Su et al., 2020).

2
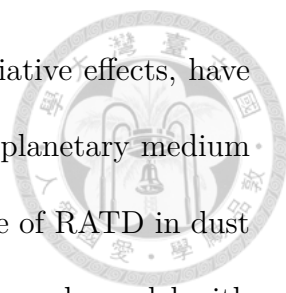
The idea that photon absorption and emission could induce rapid grain rotation was initially proposed by Harwit (1970), though their model was based on a random-walk process of photon angular momentum transfer. Later, Dolginov & Mitrofanov (1976) proposed that differential absorption and scattering of radiation by helical grains could generate radiative torques, leading to grain alignment. Numerical calculations by Draine & Weingartner (1997) confirmed that radiative torques (RATs) are significant for irregularly shaped grains, capable of spinning them up to superthermal rotation, where the angular momentum J exceeds its thermal equilibrium value. Lazarian & Hoang (2007) developed an analytical model for RATs, and Hoang & Lazarian (2008) showed that grains can align at either low-J or high-J attractor points, with the fraction of grains at high-J states (f_{highJ}) depending on parameters such as radiation field intensity, grain size, shape, charge distribution, and magnetic properties (Hoang & Lazarian, 2016; Hoang et al., 2023).

Hoang et al. (2019) first proposed that large grains aligned at high-J attractors could be fragmented into smaller particles if the centrifugal force generated by suprathermal rotation exceeds the binding force holding the grain together (see also Hoang, 2019). More recently, Hoang et al. (2021) demonstrated that the Radiative Torque Disruption (RATD) mechanism can efficiently produce nanoparticles by fragmenting large dust grains in the F-corona, offering an explanation for the observed decrease in F-coronal dust density with distance from the Sun. However, the impact of RATD on dust fragmentation beyond the F-corona in the heliosphere remains unexplored.

This thesis investigates whether nanoparticles can also be produced through RATD-driven fragmentation of larger dust grains ($> 0.1\,\mu$m) in the Solar System

environment. Several key processes, including collisions and radiative effects, have been incorporated into models of dust size evolution in the interplanetary medium (see Mann, 2017, for a review). In this work, we examine the role of RATD in dust size distribution by incorporating it into a simplified collisional cascade model with Poynting-Robertson drag. Additionally, we conduct a preliminary analysis of the rotational disruption of micrometer-sized particles strongly affected by radiation pressure. Despite the simplified nature of our model, this study aims to provide insights into the potential impact of RATD on heliospheric dust.

The structure of this thesis is organized into five chapters, each addressing a specific aspect of the research. In Chapter 2, we review the theoretical foundation of RATD, including equations for rotational and collisional disruption timescales, and discuss key heliospheric parameters. We also introduce a simplified model for computing the dust grain size distribution. In Chapter 3, we apply RATD theory to dust in the heliosphere, calculating disruption grain sizes and timescales and analyzing the resulting size distribution under different tensile strengths and grain alignment fractions. We further explore the implications of RATD for constraining the present-day location of the water snow line. In Chapter 4, we discuss the effects of radiation pressure and propose potential future experimental tests. Finally, Chapter 5 summarizes our findings. Additional derivations are provided in the appendices: Appendix 5 derives the general rotational timescale for a dust grain damped by hydrogen gas, Appendix 5 derives the radiation pressure cross-section, and Appendix 5 introduces and compares the magnitudes of various torques arising from alignment mechanisms.

Chapter 2 Theoretical Foundation of RATD

In this section, we review the theoretical framework of Radiative Torque Disruption (RATD), as proposed by Hoang et al. (2019). RATD has been extensively studied in various astrophysical environments and validated through observational constraints (see Tram & Hoang, 2022).

The core principle of RATD is that radiative torques can align and spin up dust grains to suprathermal rotation at stable attractor points of high angular momentum (hereafter high-J attractors) (Hoang & Lazarian, 2008; Lazarian & Hoang, 2007). When the rotational velocity becomes sufficiently high, centrifugal forces overcome the grain's material strength, leading to its fragmentation into smaller particles.

However, competing mechanisms such as gas collisions and infrared emission act to slow down the grain's rotation. The relative timescales of these processes determine the effectiveness of RATD and play a crucial role in shaping the final size distribution of dust grains in different astrophysical environments.

2.1 Radiation Field, Gas, and Dust Properties in the Heliosphere

The energy density of the radiation field is defined as

$$u_{\text{rad}} = \int u_\lambda d\lambda.$$

(2.1)

We introduce the dimensionless parameter U, which quantifies the radiation energy density relative to the interstellar radiation field (ISRF):

$$U = \frac{u_{\text{rad}}}{u_{\text{ISRF}}},$$

(2.2)

where the ISRF energy density is $u_{\text{ISRF}} = 8.64 \times 10^{-13} \, \text{erg cm}^{-3}$ (Mathis et al., 1983). In the Solar System, the radiation field strength varies with heliocentric distance as

$$U \approx 5.2 \times 10^7 \left(\frac{r}{1 \, \text{au}} \right)^{-2}.$$

(2.3)

The Sun's radiation intensity depends on its surface temperature, which we assume to be $5800 \, \text{K}$, treating it as a perfect blackbody emitter. The corresponding radiation energy density at a heliocentric distance r is

$$u_{\text{rad}} = 4.62 \times 10^{-5} \left(\frac{r}{1 \, \text{au}} \right)^{-2} \, \text{erg cm}^{-3}.$$

(2.4)

The mean wavelength of radiation can be estimated as

$$\bar{\lambda} = \frac{\int \lambda u_\lambda d\lambda}{u_{\text{rad}}} = 9.18 \times 10^{-5} \, \text{cm}.$$

(2.5)

Inside the heliosphere ($r < 100\,\mathrm{au}$), hydrogen gas originates from two primary sources: the solar wind and the Local Interstellar Medium (LISM). The ROSAT mission provided the first all-sky survey of soft X-ray emission from the LISM, and the Ulysses mission further constrained its properties (Egger et al., 1996). Within the heliosphere, a fraction of interstellar dust can be ionized due to photoionization and charge exchange with the solar wind (Geiss et al., 1996; Izmodenov & Kallenbach, 2006).

The number density of solar wind protons follows an inverse square law:

$$n_{\mathrm{p}}(\mathrm{SW}) = 7\left(\frac{r}{1\,\mathrm{au}}\right)^{-2}\ \mathrm{cm}^{-3} \tag{2.6}$$

(Baranov & Malama, 1995; Gopalswamy et al., 2010). Meanwhile, the LISM hydrogen number density is approximately

$$n_{\mathrm{H}}(\mathrm{LISM}) = 0.09\,\mathrm{cm}^{-3} \tag{2.7}$$

for regions beyond $10\,\mathrm{au}$ (Gopalswamy et al., 2010). Inside $10\,\mathrm{au}$, the LISM contribution becomes negligible compared to the solar wind.

The temperatures and drift velocities of the solar wind and LISM hydrogen atoms are given by:

$$T(\mathrm{SW}) \simeq 8.3 \times 10^4\,\mathrm{K}, \qquad\qquad T(\mathrm{LISM}) \simeq 6306\,\mathrm{K}, \tag{2.8}$$

$$v(\mathrm{SW}) \simeq 500\,\mathrm{km/s}, \qquad\qquad v(\mathrm{LISM}) \simeq 26.24\,\mathrm{km/s} \tag{2.9}$$

(Baranov & Malama, 1995; Izmodenov & Kallenbach, 2006). Since protons and hydrogen atoms have nearly identical masses, the rotational damping time of a dust

grain in both gases is similar (see Equation 2.19). To generalize, we define the weighted mean for a physical quantity q as:

$$\bar{q} = \frac{n_p(\text{SW})}{n_H} q(\text{SW}) + \frac{n_H(\text{LISM})}{n_H} q(\text{LISM}), \qquad (2.10)$$

where n_H is the total number density of solar wind protons and LISM hydrogen atoms.

Cosmic dust in the Solar System is classified into three main populations: interstellar dust (ISD), interplanetary dust particles (IDP), and circumplanetary dust. This study focuses on ISD and IDP, as circumplanetary dust has complex orbital dynamics and rotational damping behavior that depend on planetary atmospheres.

ISD originates from the Local Interstellar Cloud (LIC) and traverses the Solar System due to the relative velocity between the Sun and the LIC, which is approximately $26\,\text{km s}^{-1}$ (McComas et al., 2015). At the heliosphere's boundary, ISD particles with high charge-to-mass ratios are filtered by the Lorentz force. Simulations indicate that ISD grains smaller than $0.01\,\mu\text{m}$ are entirely excluded (Slavin et al., 2012; Sterken et al., 2019).

IDPs, on the other hand, originate from asteroids, comets, and the Kuiper Belt (Keller & Flynn, 2022; Mann, 2017). Within $3\,\text{au}$, IDPs form zodiacal dust bands, which contribute to zodiacal light (Jorgensen et al., 2021).

The cumulative flux of interplanetary dust at $r_0 = 1\,\text{au}$ follows (Mann et al., 2004):

$$F(m, r_0) = (c_1 m^{g_1} + c_2)^{g_2} + c_3(m + c_4 m^{g_3} + c_5 m^{g_4})^{g_5} + c_6(m + c_7 m^{g_6})^{g_7}, \qquad (2.11)$$

8

where constants c_i and g_i are fitted from observational data.

Regarding the radial dependence of dust number density, observations suggest that zodiacal cloud grains originate from multiple sources and their density varies with heliocentric distance (Jorgensen et al., 2021; Rowan-Robinson & May, 2013). For simplicity, we assume a power-law distribution:

$$n(r) \propto r^{-\nu}, \quad \nu = 1.3 \tag{2.12}$$

(Divine, 1993; Leinert et al., 1981). The flux variation for low-eccentricity orbits is approximated as:

$$F(m, r) = F(m, r_0)\left(\frac{r}{r_0}\right)^{-1.8}. \tag{2.13}$$

2.2 Theory of Radiative Torque

Radiative torque (RAT) arises from the interaction between an anisotropic radiation field and an irregularly shaped dust grain. This mechanism plays a crucial role in the rotational dynamics of interstellar and interplanetary dust grains. The magnitude of the RAT exerted on a dust grain depends on its size, the anisotropy of the radiation field, and the radiation's spectral properties.

For a dust grain with an effective radius a, defined as the radius of a sphere with an equivalent volume, the RAT is given by Draine & Weingartner (1997):

$$\Gamma_{\text{RAT}} = \pi a^2 \gamma_{\text{rad}} u_{\text{rad}} \left(\frac{\bar{\lambda}}{2\pi}\right) \langle Q_\Gamma \rangle, \tag{2.14}$$

where u_{rad} represents the radiation energy density, and γ_{rad} is the anisotropy degree

9

of the radiation field. The mean wavelength $\bar{\lambda}$ of the radiation field is defined as:

$$\bar{\lambda} = \frac{\int \lambda u_\lambda d\lambda}{u_{\text{rad}}},$$

(2.15)

and the spectral-averaged RAT efficiency, $\langle Q_\Gamma \rangle$, is given by:

$$\langle Q_\Gamma \rangle = \frac{\int Q_\Gamma \lambda u_\lambda d\lambda}{\int \lambda u_\lambda d\lambda}.$$

(2.16)

Inside the heliosphere, where the radiation field is highly anisotropic, the anisotropy parameter is $\gamma_{\text{rad}} \approx 1$. The spectral-averaged RAT efficiency, $\langle Q_\Gamma \rangle$, can be approximated using the empirical relation given by Hoang (2019):

$$\langle Q_\Gamma \rangle \simeq \begin{cases} 2\left(\frac{\bar{\lambda}}{a}\right)^{-2.7}, & a \lesssim \bar{\lambda}/1.8, \\[2ex] 0.4, & a > \bar{\lambda}/1.8. \end{cases}$$

(2.17)

Substituting Equation (2.17) into Equation (2.14), the RAT is obtained as:

$$\Gamma_{\text{RAT}} \simeq \begin{cases} 5.8 \times 10^{-29} a_{-5}^{4.7} \gamma_{\text{rad}} U \bar{\lambda}_{0.5}^{-1.7} \text{ dyne cm}, & a \lesssim \bar{\lambda}/1.8, \\[2ex] 8.6 \times 10^{-28} a_{-5}^2 \gamma_{\text{rad}} U \bar{\lambda}_{0.5} \text{ dyne cm}, & a > \bar{\lambda}/1.8. \end{cases}$$

(2.18)

Here, the normalized parameters are defined as $a_{-5} = a/10^{-5}$ cm and $\bar{\lambda}_{0.5} = \bar{\lambda}/0.5\,\mu\text{m}$.

These expressions provide a quantitative framework for understanding the influence of radiative torques on dust grains under different radiation conditions. The RAT efficiency depends strongly on the grain size relative to the mean wavelength, which determines whether the torque scales as $a^{4.7}$ or a^2. This scaling plays a critical role in modeling the rotational dynamics of dust grains in astrophysical

environments.

2.3 Rotational Damping Mechanisms and Timescales

Rotational damping can be divided into several different processes, including neutral impacts, ion impacts, thermal emission of infrared photons, and rotational dipole emission (Draine & Lazarian, 1998).

Here, we calculate the general damping timescale of a dust grain damped by hydrogen gas as follows (see Appendix 5):

$$\overline{\tau}_{\mathrm{H}}(v_{\mathrm{d}}, v_{\mathrm{th}}) = \frac{3I}{2n_{\mathrm{H}}m_{\mathrm{H}}a^4\overline{v_{\mathrm{th}}K(s)}}, \tag{2.19}$$

where the bar notation denotes the weighted mean in Equation 2.10 and will be omitted afterward, n_{H} is the total number density of protons, v_{d} is the drift velocity of dust grains with respect to the gas, $v_{\mathrm{th}} = (2kT_{\mathrm{gas}}/m_{\mathrm{H}})^{1/2}$ is the thermal gas velocity, $K(s) = 2\sqrt{\pi} + \pi s + \pi(e^{-s} - 1)$ and $s = v_{\mathrm{d}}/v_{\mathrm{th}}$.

The above approximation is convenient for numerical calculation, as it covers both high and low sound speeds in one equation. For instance, for zodiacal dust, the average drift velocity is much larger than the thermal velocity for protons in the solar wind, $v_{\mathrm{d}} \gg \bar{v}_{\mathrm{th}}$ for $T_{\mathrm{gas}} = 83\,000\,\mathrm{K}$ and $v_{\mathrm{d}} = 500\,\mathrm{km/s}$. On the other hand, the average drift velocity and thermal velocity are around $26\,\mathrm{km/s}$ according to Lyman-α observations (Izmodenov & Kallenbach, 2006) for dust colliding with neutral gas in the LISM which dominates within $10\,\mathrm{au}$ to $100\,\mathrm{au}$. Therefore, this example shows the importance of considering dust grains colliding with different sources of gas.

To facilitate comparisons across different sources of rotational damping, we adopt τ_{H} with $v_{\mathrm{d}} = 0$ as a fiducial timescale. The damping time due to process j is expressed as:

$$\tau_j^{-1} = F_j \tau_{\mathrm{H}}^{-1}, \tag{2.20}$$

and the total damping time is:

$$\tau_{\mathrm{damp}}^{-1} = (F_n + F_i + F_{\mathrm{IR}} + F_{\mathrm{ed}}) \, \tau_{\mathrm{H}}^{-1}, \tag{2.21}$$

where F_n, F_i, F_{IR}, and F_{ed} are the contributions from neutral imparts, ion impacts, thermal emission of infrared photons, and rotational dipole emission, respectively. For gas with He of 10% abundance, $F_n + F_i \simeq 1.2$ (Draine & Lazarian, 1998).

The contributions due to the rotational dipole emission (F_{ed}) can be rewritten as (Draine & Lazarian, 1998; Hoang et al., 2016):

$$F_{\mathrm{ed}} = \left(\frac{I\omega^2}{3kT_{\mathrm{d}}} \right) \frac{\tau_{\mathrm{H}}}{\tau_{\mathrm{ed}}}, \tag{2.22}$$

where T_{d} is the dust temperature, and characteristic damping time τ_{ed} is defined as:

$$\tau_{\mathrm{ed}} = \frac{3I^2 c^3}{6kT_{\mathrm{gas}}\mu_e^2}. \tag{2.23}$$

As we will see in Section 2.5, a dust grain is disrupted when its angular velocity, ω, exceeds the critical rotational velocity, ω_{disr}. To estimate the upper bound of the rotational dipole emission, F_{ed}, we substitute ω with ω_{disr}. By incorporating Equations 2.19, 2.23, and 2.28 into Equation 2.22, the expression for F_{ed} is derived

as:

$$F_{\text{ed}} = 1.4 \times 10^{-3} \left(\frac{S_{\text{max},9}}{a_{-5}^2 \hat{\rho}} \right) \left(\frac{30 \, \text{cm}^{-3}}{n_{\text{H}}} \right) \left(\frac{T_{\text{d}}}{15 \, \text{K}} \right)^{-1} \left(\frac{V}{3 \, \text{V}} \right)^2 \left(\frac{T_{\text{gas}}}{100 \, \text{K}} \right)^{1/2} \left(\frac{2 \sqrt{\pi}}{K(s)} \right), \quad (2.24)$$

where $a_{-5} = a/(10^{-5} \, \text{cm})$, $\hat{\rho} = \rho/(3 \, \text{g cm}^{-3})$, and $S_{\text{max},9} = S_{\text{max}}/(10^9 \, \text{erg cm}^{-3})$.

Finally, the IR damping coefficient is (Draine & Lazarian, 1998):

$$F_{\text{IR}} \approx \left(\frac{0.4 U^{2/3}}{a_{-5}} \right) \left(\frac{30 \, \text{cm}^{-3}}{n_{\text{H}}} \right) \left(\frac{100 \, \text{K}}{T_{\text{gas}}} \right)^{1/2} \left(\frac{2 \sqrt{\pi}}{K(s)} \right). \quad (2.25)$$

Notably, $\tau_{\text{IR}} = F_{\text{IR}} \tau_{\text{H}}^{-1}$ remains independent of gas temperature T_{gas} and density n_{H}. Furthermore, as demonstrated in Hoang (2019) and Lazarian & Hoang (2007), for a dust grain that is trapped in high-J attractor points, equilibrium rotation is attained at:

$$\omega_{\text{RAT}} = \frac{\Gamma_{\text{RAT}} \tau_{\text{damp}}}{I}, \quad (2.26)$$

where $I = 8\pi \rho a^5/15$, $\rho = 3 \, \text{g cm}^{-3}$ are the moment of inertia and the typical density of the grain, respectively.

Using the parameters $S_{\text{max},9} = 1$, $\hat{\rho} = 1$, and $T_{\text{d}} = 15 \, \text{K}$, Fig. 2.1 compares the damping coefficient due to thermal emission of infrared photons (F_{IR}, solid lines; see Equation 2.25) and rotational dipole emission (F_{ed}, dashed lines; see Equation 2.24) across different grain sizes (a) and heliocentric distances (r). The figure illustrates that, within heliocentric distances ranging from $0.1 \, \text{au}$ to $100 \, \text{au}$ and for grain sizes larger than $0.1 \, \mu\text{m}$, F_{IR} dominates over F_{ed}. Consequently, F_{ed} can be neglected in the regions under consideration.
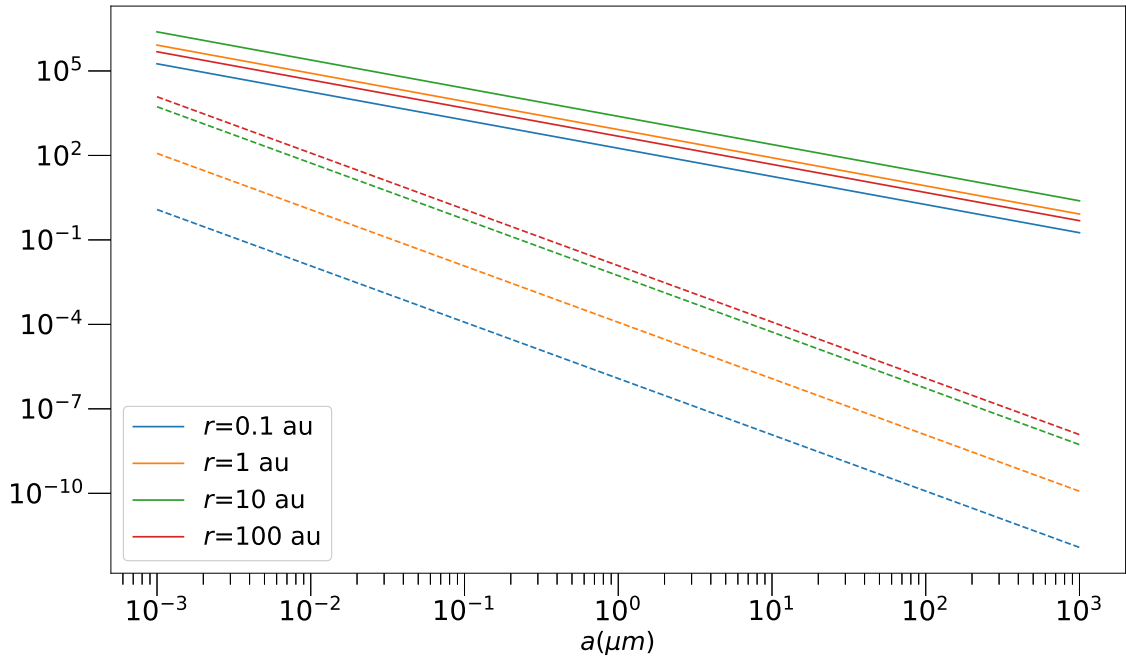
Figure 2.1: Comparison of damping coefficient due to thermal emission of infrared photons (F_{IR}, solid lines; see Equation 2.25) and rotational dipole emission (F_{ed}, dashed lines; see Equation 2.24) for different grain sizes (a) and heliocentric distances (r).

2.4 Tensile Strength of Dust Grains in the Heliosphere

The tensile strength of dust particles in the heliosphere spans several orders of magnitude, depending on their composition, structure, and physical properties. Analyses of meteoroid atmospheric entries (typically "cometary" dust) suggest very low tensile strengths of approximately $\sim 4{\times}10^3$–10^5 dyn cm^{-2} (Musiolik et al., 2017), consistent with extremely fragile, loosely-bound aggregate structures.

For silicate-based dust (e.g., olivine, pyroxene, granite), both laboratory experiments and modeling studies indicate tensile strengths in the range of 10^3–10^6 dyn cm^{-2} (Gundlach et al., 2018; Haack et al., 2020; Kimura et al., 2020), primarily reflecting the properties of silica-rich materials.

Carbonaceous dust, such as organic-rich interplanetary dust particles (IDPs)

and carbonates, exhibit significantly higher strengths. Micro-compression experiments on $\sim 100\,\mu m$ fragments of CM/CI chondrites (rich in organics) have revealed tensile strengths in the range of 3×10^6–3×10^8 dyn cm^{-2} (Musiolik et al., 2017; Tsuchiyama et al., 2009).

In the case of ice-rich dust (e.g., water ice or ice–dust mixtures), pure water ice exhibits relatively high tensile strength at low temperatures. For instance, uniaxial compression tests yield values of $\sim 5 \times 10^6$–1.3×10^7 dyn cm^{-2} near 150 K (Zhang et al., 2022). However, the surface layers of cometary nuclei are much weaker; for comet 67P, modeling and Rosetta mission data suggest that the dusty ice crust has tensile strengths of only 30–1500 dyn cm^{-2}, low enough that sublimation pressures of a few pascals can lift material (Tatsuuma et al., 2019).

Metal-rich dust grains, such as iron–nickel (FeNi) fragments from asteroid disruption, are among the strongest. Tensile tests on iron meteorite samples yield strengths as high as $\sim 5.6 \times 10^9$ dyn cm^{-2} (Ahles et al., 2021).

2.5   Critical Rotational Velocity and Disruption Thresholds

A rotating dust grain of size a and angular velocity ω experiences a centrifugal stress, which is given by:

$$S = \frac{\rho a^2 \omega^2}{4},\tag{2.27}$$

where ρ is the material density of the grain (Hoang, 2019). The critical rotational velocity, ω_{disr}, represents the threshold at which centrifugal stress overcomes the grain's internal cohesive forces. When this stress equals the maximum tensile strength $S_{\max}$ (which varies by composition and internal structure), fragmentation occurs. This

15

critical velocity is given by:

$$\omega_{\text{disr}} = \frac{2}{a}\left(\frac{S_{\text{max}}}{\rho}\right)^{1/2}$$

$$\simeq 3.6 \times 10^9 a_{-5}^{-1}\hat{\rho}^{-1/2}S_{\text{max},9}^{1/2} \text{ rad/s}, \tag{2.28}$$

where $a_{-5} = a/(10^{-5}\,\text{cm})$, $\hat{\rho} = \rho/(3\,\text{g cm}^{-3})$, and $S_{\text{max},9} = S_{\text{max}}/(10^9\,\text{erg cm}^{-3})$.

The values of $\hat{\rho}$ and S_{max} can vary significantly depending on the grain's material properties. For reference, bulk ice has $\hat{\rho} = 0.306$ and $S_{\text{max}} = 1 \times 10^7\,\text{dyn cm}^{-2}$ (Petrovic, 2003), while cast iron has $\hat{\rho} = 2.4$ and $S_{\text{max}} = 2 \times 10^9\,\text{dyn cm}^{-2}$. Monocrystalline silicon exhibits $\hat{\rho} = 0.776$ and $S_{\text{max}} = 7 \times 10^{10}\,\text{dyn cm}^{-2}$, with additional values found in Howatson et al. (1972).

A dust grain undergoes rotational disruption if $\omega_{\text{disr}} < \omega_{\text{RAT}}$, which leads to the condition:

$$\frac{2}{a}\left(\frac{S_{\text{max}}}{\rho}\right)^{1/2} < \frac{\Gamma_{\text{RAT}}\tau_{\text{damp}}}{I}. \tag{2.29}$$

From this, the disruption size thresholds are derived:

$$a_{-5}^{1.7} > 7.02 \times 10^{-7}\hat{\rho}^{-1/2}S_{\text{max},9}^{1/2}\gamma_{\text{rad}}^{-1}\bar{\lambda}_{0.5}^{1.7}\times \tag{2.30}$$

$$\frac{n_{\text{H}}(1.2 + F_{\text{IR}})v_{\text{th}}K(s)}{U},$$

for grains with $a \lesssim \bar{\lambda}/1.8$, and

$$a_{-5} < 2.1 \times 10^7\hat{\rho}^{1/2}S_{\text{max},9}^{-1/2}\gamma_{\text{rad}}\bar{\lambda}_{0.5}\frac{U}{n_{\text{H}}(1.2 + F_{\text{IR}})v_{\text{th}}K(s)}, \tag{2.31}$$

for grains with $a > \bar{\lambda}/1.8$.

Equations (2.30) and (2.31) define the range of grain sizes subject to rotational

16

disruption. The upper limit in Equation (2.31) arises from the increasing moment of inertia for larger grains, while the lower limit in Equation (2.30) is due to the decreasing cross-sectional area.
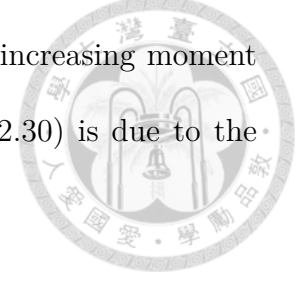
Under the assumption of a strong solar radiation field within the heliosphere, where $F_{\mathrm{IR}} \gg 1$, Equation (2.30) simplifies to:

$$a_{\mathrm{disr,min}} \simeq 0.16 \left(\gamma_{\mathrm{rad}}^{-1} U^{-1/3} \bar{\lambda}_{0.5}^{1.7} S_{\mathrm{max,9}}^{1/2} \right)^{1/2.7} \ \mu\mathrm{m}, \qquad (2.32)$$

for grains with $a \lesssim \bar{\lambda}/1.8$. As expected, the minimum disruption size is independent of gas density and temperature in the first-order approximation.

Similarly, the maximum disruption grain size is found by solving Equation (2.31):

$$a_{\mathrm{disr,max}} \simeq \left(0.46 \gamma_{\mathrm{rad}} \bar{\lambda}_{0.5} \hat{\rho}^{1/2} S_{\mathrm{max,9}}^{-1/2} \frac{U}{\hat{n}_{\mathrm{H}} \hat{T}^{1/2} K(s)} - \frac{U^{2/3}}{30 \hat{n}_{\mathrm{H}}} \frac{2\sqrt{\pi}}{\hat{T}^{1/2} K(s)} \right) \ \mu\mathrm{m}, \qquad (2.33)$$

where $\hat{T}^{1/2} = T_{\mathrm{gas}}/100\,\mathrm{K}$ and $\hat{n}_{\mathrm{H}} = n_{\mathrm{H}}/30\,\mathrm{cm}^{-3}$. Under the strong radiation field assumption, the second term can be neglected, yielding:

$$a_{\mathrm{disr,max}} \simeq 0.46 \gamma_{\mathrm{rad}} \bar{\lambda}_{0.5} \hat{\rho}^{1/2} S_{\mathrm{max,9}}^{-1/2} \frac{U}{\hat{n}_{\mathrm{H}} \hat{T}^{1/2} K(s)} \ \mu\mathrm{m}. \qquad (2.34)$$

The maximum disruption size depends on gas temperature and density, as $F_{\mathrm{IR}} \gg 1$ no longer holds for $a \approx a_{\mathrm{disr,max}}$.

As detailed in Hoang et al. (2019), the equation of motion for irregular grains

17

subjected to RATs and rotational damping is given by:

$$\frac{I d\omega}{dt} = \Gamma_{\text{RAT}} - \frac{I\omega}{\tau_{\text{damp}}}.$$ (2.35)

The corresponding disruption timescale is:

$$t_{\text{disr}} = -\tau_{\text{damp}} \ln\left(1 - \frac{\omega_{\text{disr}}}{\omega_{\text{RAT}}}\right).$$ (2.36)

For cases where the damping time is much greater than the disruption time ($\omega_{\text{RAT}} \gg \omega_{\text{disr}}$) or when rotational damping is negligible ($\tau_{\text{damp}} \to \infty$), the characteristic disruption timescale is:

$$t_{\text{disr},0} = \frac{I\omega_{\text{disr}}}{\Gamma_{\text{RAT}}}$$ (2.37)

$$\simeq 37.2(\gamma U_7)^{-1}\bar{\lambda}_{0.5}^{1.7}\hat{\rho}^{1/2}S_{\text{max},9}^{1/2}a_{-5}^{-0.7} \text{ days,}$$ (2.38)

for $a \lesssim \bar{\lambda}/1.8$, and

$$t_{\text{disr},0} \simeq 2.46(\gamma U_7)^{-1}\bar{\lambda}_{0.5}^{-1}\hat{\rho}^{1/2}S_{\text{max},9}^{1/2}a_{-5}^{2} \text{ days,}$$ (2.39)

for $a > \bar{\lambda}/1.8$. The condition $\omega_{\text{disr}} < \omega_{\text{RAT}}$ ensures that $t_{\text{disr},0} < \tau_{\text{damp}}$.

2.6 RAT-Driven Grain Dynamics: High-J and Low-J Attractor

In Equation 2.14, it is assumed that the radiation direction is aligned with the angular momentum vector **J**, and due to symmetry, the averaged RATD is also aligned with the radiation direction. However, this alignment is not generally

18
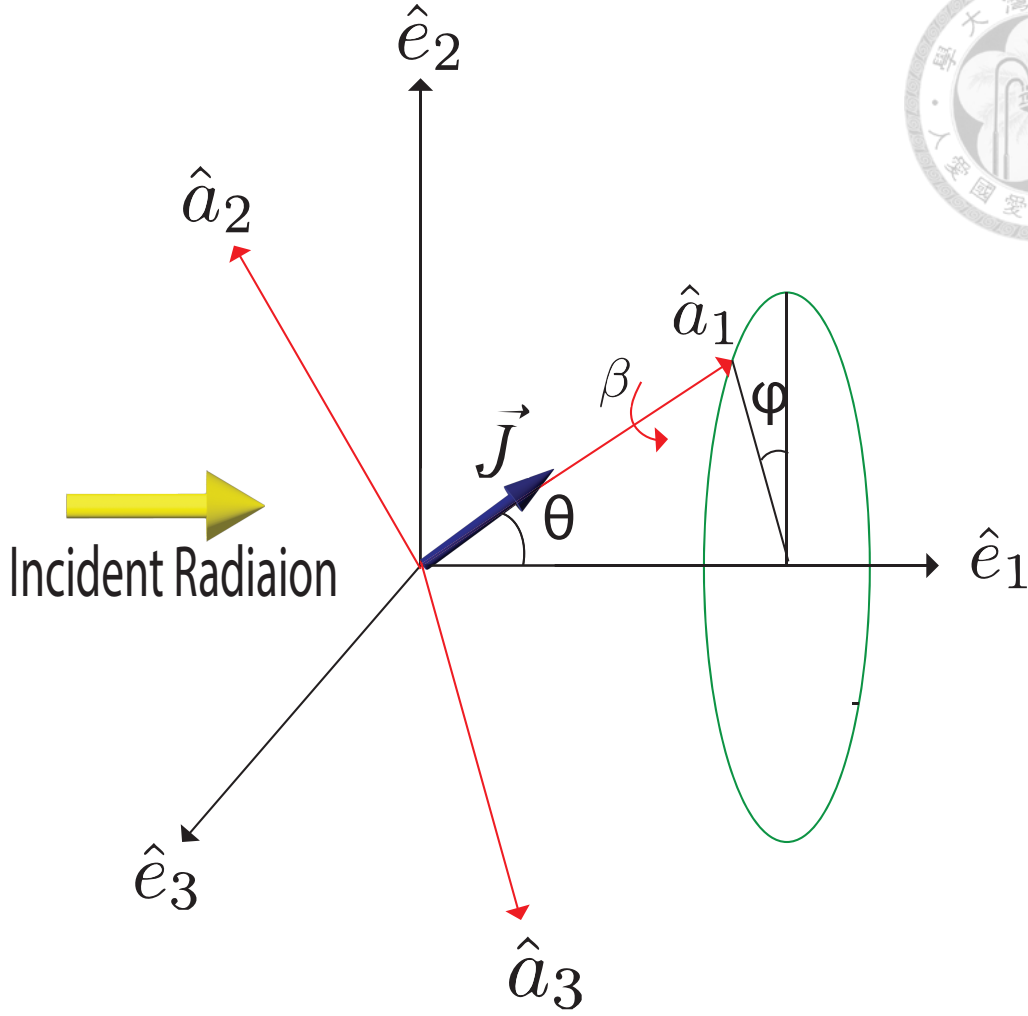
Figure 2.2: The orientation of a grain is described by three angles θ, ϕ, and β. The grain's body frame is defined by the principal axes a_1, a_2, and a_3, while the laboratory frame (scattering reference system) is described by e_1, e_2, and e_3. The incident radiation is directed along e_1. The angular momentum vector $\mathbf{J}$ is assumed to be coupled to the principal axis a_1 of maximum inertia.

valid. In most realistic scenarios, the radiation direction is not parallel to the angular momentum vector $\mathbf{J}$. Under these conditions, the torque expression in Equation 2.14 must be revised to reflect the misalignment:

$$\mathbf{\Gamma}_{\text{RAT}}(\theta, \phi, \beta) = \pi a^2 \gamma_{\text{rad}} u_{\text{rad}} \left(\frac{\bar{\lambda}}{2\pi} \right) \mathbf{Q}_{\Gamma}(\theta, \phi, \beta). \tag{2.40}$$

As illustrated in Fig. 2.2, θ is the angle between the maximum moment of inertia axis a_1 and the incident light direction e_1, ϕ is the precession angle of a_1 about e_1,

and β is the grain rotation angle around a_1. Due to symmetry, the angle ϕ can be neglected. Therefore, Equation 2.41 simplifies to:

$$\mathbf{\Gamma}_{\mathrm{RAT}}(\theta, \beta) = \pi a^2 \gamma_{\mathrm{rad}} u_{\mathrm{rad}} \left(\frac{\bar{\lambda}}{2\pi} \right) \mathbf{Q}_{\Gamma}(\theta, \beta). \tag{2.41}$$

To further simplify, we assume a_1 and $\mathbf{J}$ are coupled due to fast rotation and efficient internal relaxation (Lazarian & Draine, 1999; Purcell, 1979). This enables averaging over β:

$$\langle \mathbf{\Gamma}_{\mathrm{RAT}} \rangle (\theta) = \pi a^2 \gamma_{\mathrm{rad}} u_{\mathrm{rad}} \left(\frac{\bar{\lambda}}{2\pi} \right) \langle \mathbf{Q}_{\Gamma} \rangle (\theta). \tag{2.42}$$

Here, $\langle \cdot \rangle$ denotes an average over β. The radiation torque can be decomposed along $\hat{a}_1$, $\hat{\theta}$, and $\hat{\phi}$ directions:

$$\langle \mathbf{\Gamma}_{\mathrm{RAT}} \rangle (\theta) = \left\langle \Gamma_{\mathrm{RAT,a_1}} \right\rangle (\theta) \hat{a}_1 + \left\langle \Gamma_{\mathrm{RAT},\theta} \right\rangle (\theta) \hat{\theta} + \left\langle \Gamma_{\mathrm{RAT},\phi} \right\rangle (\theta) \hat{\phi}. \tag{2.43}$$

The equations of motion are then expressed as:

$$\frac{dJ}{dt} = M \left\langle \Gamma_{\mathrm{RAT,a_1}} \right\rangle (\theta) - J \tag{2.44}$$

$$\frac{d\theta}{dt} = M \frac{\left\langle \Gamma_{\mathrm{RAT},\theta} \right\rangle (\theta)}{J}, \tag{2.45}$$

where time t and angular momentum J are scaled by the gas damping time t_{damp} and thermal angular momentum $I_1 \omega_{\mathrm{T}}$, with I_1 being the moment of inertia about a_1, and $\omega_T = \left(\frac{k T_{\mathrm{gas}}}{I_1} \right)^{1/2}$.

The stationary points are determined by setting the equations of motion 2.44 and 2.45 equal to zero. A stationary point becomes an attractor if the following
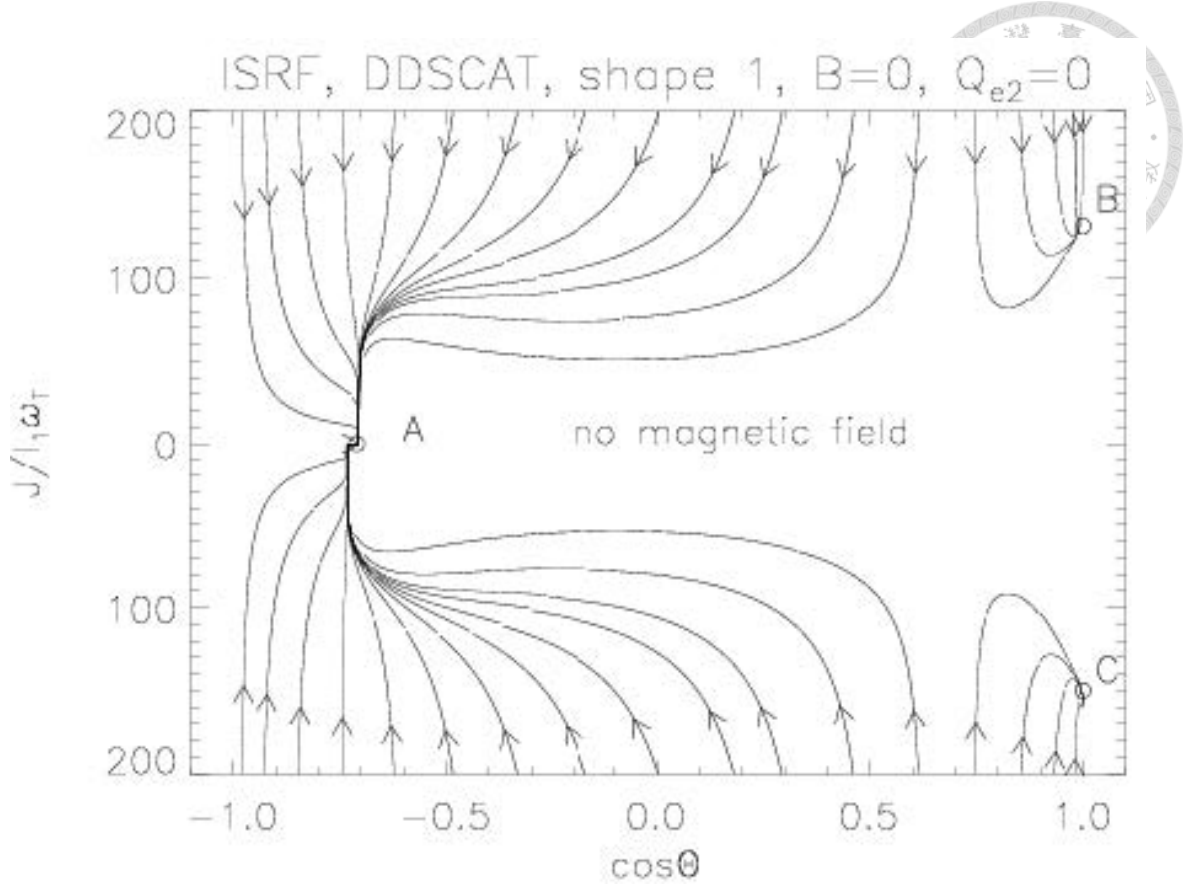
Figure 2.3: A representative phase trajectory map showing three attractor points: A, B, and C. Points B and C correspond to high angular momentum states (high-J attractors), while point A corresponds to a low angular momentum state (low-J attractor) (Lazarian & Hoang, 2007).

conditions are satisfied at $\theta = \theta_s$ (Lazarian & Hoang, 2007):

$$
\left.\frac{d\left\langle\Gamma_{\mathrm{RAT},\theta}\right\rangle(\theta)}{d\theta}\right|_{\theta=\theta_s} < 0, \quad \text{for } \left\langle\Gamma_{\mathrm{RAT},a_1}\right\rangle(\theta_s) > 0 \tag{2.46}
$$

$$
\left.\frac{d\left\langle\Gamma_{\mathrm{RAT},\theta}\right\rangle(\theta)}{d\theta}\right|_{\theta=\theta_s} > 0, \quad \text{for } \left\langle\Gamma_{\mathrm{RAT},a_1}\right\rangle(\theta_s) < 0 \tag{2.47}
$$

Given a specific grain, one can compute the torque components $\left\langle\Gamma_{\mathrm{RAT},\theta}\right\rangle(\theta)$ and $\left\langle\Gamma_{\mathrm{RAT},a_1}\right\rangle(\theta)$. Phase trajectory maps such as in Fig. 2.3 help visualize these attractor points in angular momentum space, clearly distinguishing high-J attractors (points B and C) from low-J attractors (point A).

2.7 Impact of Ice Mantles on Rotational Disruption

The presence of ice mantles on dust grains plays a crucial role in their structural integrity and rotational dynamics. These ice mantles can form through heterogeneous condensation processes in low-temperature interstellar clouds, as described by Seki & Hasegawa (1983). The structural properties of such icy layers have been extensively studied by Hoang & Tram (2020), who demonstrated that water vapor condensation leads to the formation of a layered structure on the surface of the grain core.

To analyze the rotational disruption of ice-mantled grains, we adopt a simplified model in which the dust grain is assumed to be a sphere of radius a. The average tensile strength of a rotating sphere at a distance R from its center is given by Kadish et al. (2005):

$$S(R) = \frac{\rho \omega^2 (a^2 - R^2)}{4}.$$

(2.48)

Here, we assume that the adhesion strength between the ice mantle and the core is equal to the tensile strength of ice. Given that the tensile strength of the core is significantly higher than that of the outer ice layer, the outer layer is expected to break first under centrifugal force. The critical rotational velocity at which this occurs is determined by setting $S = S_{\max}$:

$$\omega_{\text{disr}} = \left(\frac{4S_{\max}}{\rho(a^2 - R^2)}\right)^{1/2}$$

$$\simeq 3.6 \times 10^9 (a^2 - R^2)^{-1/2} a_{-5}^{-1} \hat{\rho}^{-1/2} S_{\max,9}^{1/2} \text{ rad/s.} \tag{2.49}$$

By comparing this result to Equation 2.28, we find that the effective tensile strength of the ice mantle is modified as follows:

$$S_{\text{eff}} = \frac{S_{\max}}{1 - (R/a)^2}. \tag{2.50}$$

Substituting $S_{\max}$ with S_{eff} in Equations 2.32 and 2.34, we obtain the expressions for the minimum and maximum disruption sizes in the ice mantle model:

$$a_{\text{disr,min}} \simeq \frac{0.16}{[1 - (R/a)^2]^{1/5.4}} \left(\gamma_{\text{rad}}^{-1} U^{-1/3} \bar{\lambda}_{0.5}^{1.7} S_{\max,9}^{1/2}\right)^{1/2.7} \ \mu\text{m}, \tag{2.51}$$

$$a_{\text{disr,max}} \simeq 0.46 \gamma_{\text{rad}}^{-1} \bar{\lambda}_{0.5} \hat{\rho}^{1/2} \left[1 - (R/a)^2\right]^{1/2} S_{\max,9}^{-1/2} \frac{U}{\hat{n}_{\text{H}}} \frac{2\sqrt{\pi}}{\hat{T}^{1/2} K(s)} \ \mu\text{m}. \tag{2.52}$$

The results indicate that the minimum disruption size of a grain in the ice mantle model is larger than that in the bulk ice model, whereas the maximum disruption size is smaller. This suggests that the presence of an ice mantle enhances the structural resilience of smaller grains while limiting the disruption of larger

grains.

Since the results for ice-mantled grains can be derived from the bulk ice sphere model by modifying the tensile strength S, we simplify our numerical calculations by assuming $R = 0$, effectively treating the ice mantle as an ice sphere.
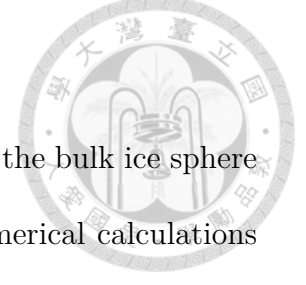
2.8   Poynting-Robertson Drag and Its Effect

The Poynting-Robertson (PR) drag plays a crucial role in the removal of nanoparticles from debris disks. This effect arises due to the momentum transfer from solar wind particles and the radiation pressure force, commonly referred to as plasma PR drag and photon PR drag, respectively. By incorporating the flux differential factor, which accounts for the discrepancy between incoming and outgoing fluxes (Grün et al., 1985), into the PR drag timescale (Hoang et al., 2021), the net mass loss timescale for a dust grain of size a in a circular debris disk at a distance r from the Sun, subject to photon differential PR drag, is given by:

$$t_{\mathrm{ph}} = \frac{4\pi\rho r^2 a c^2}{3\left\langle Q_{\mathrm{pr}}\right\rangle L_\odot} \frac{1}{\nu - 1} \approx 697 \frac{a_{-5}}{\left\langle Q_{\mathrm{pr}}\right\rangle}\left(\frac{r}{1\ \mathrm{au}}\right)^2 \ \mathrm{yrs.} \tag{2.53}$$

Here, $L_\odot$ represents the total solar energy output per second, and $\nu = 1.3$ corresponds to the exponent of the number density of dust grains, as discussed in Section 2.1. The parameters ρ and a denote the density and size of the dust grain, respectively, while c is the speed of light. The average pressure cross-section efficiency, $\left\langle Q_{\mathrm{pr}}\right\rangle$, depends on the shape and composition of the dust grain (Zubko, 2013). Theoretical values of $\left\langle Q_{\mathrm{pr}}\right\rangle$ range from 0 for perfect transmitters to 2 for

perfect backscatters, with unity for an ideal absorber (Krivov et al., 2006). For particles with a small size parameter $x = 2\pi a/\lambda \ll 1$, the pressure cross-section efficiency can be approximated as (see Appendix 5):

$$Q_{\mathrm{pr}} \simeq -4\left(\frac{2\pi a}{\lambda}\right)\Im\frac{m^2 - 1}{m^2 + 2}, \tag{2.54}$$

where m is the refractive index of the particle.

The relative importance of plasma differential PR drag compared to photon differential PR drag can be evaluated using the ratio of their timescales (Minato et al., 2006):

$$\frac{t_{\mathrm{sw}}}{t_{\mathrm{ph}}} = 3\left(\frac{\dot{M}}{\dot{M}_\odot}\right)\left(\frac{L_\odot}{L}\right)\left(\frac{Q_{\mathrm{pr}}}{Q_{\mathrm{sw}}}\right), \tag{2.55}$$

where $\dot{M}$ is the mass loss rate of the star, and $\dot{M}_\odot$ is the solar mass loss rate. Consequently, the net mass loss timescale due to plasma differential PR drag in the heliosphere is given by:

$$t_{\mathrm{sw}} = 2092\frac{a_{-5}}{\langle Q_{\mathrm{sw}}\rangle}\left(\frac{r}{1\,\mathrm{au}}\right)^2 \ \mathrm{yrs.} \tag{2.56}$$

The momentum transfer cross-section efficiency Q_{sw} follows the relation (Minato et al., 2004):

$$
Q_{\mathrm{sw}} = \begin{cases} \frac{2}{3}X & X \leq 1 \\[2ex] 1 - \frac{1}{3X^2} & X > 1 \end{cases}, \tag{2.57}
$$

where $X = 2a/l(p_0)$ is the "size parameter" [1], and p_0 is the initial momentum of an incident ion. According to SRIM (Stopping and Range of Ions in Matter) simulations, the projected ranges of protons with an initial kinetic energy of $1\,\mathrm{keV/amu}$ for SiO_2 and ice are $0.07\,\mu\mathrm{m}$ and $0.11\,\mu\mathrm{m}$, respectively (Ziegler et al., 2010). For simplicity, we assume a projected range of $l(p_0) = 0.1\,\mu\mathrm{m}$.

By comparing the timescales of plasma PR drag and photon PR drag, it is evident that photon PR drag is more efficient for larger particles ($a > 0.1\,\mu\mathrm{m}$), whereas plasma PR drag dominates for smaller particles ($a < 0.1\,\mu\mathrm{m}$) (Mann et al., 2007; Minato et al., 2004). As a result, the overall PR drag timescale is determined by the minimum of t_{ph} and t_{sw}, expressed as:

$$
t_{\mathrm{PR}} = 2092 \frac{a_{-5}}{Q_{\mathrm{eff}}} \left(\frac{r}{1\,\mathrm{au}} \right)^2 \ \mathrm{yrs}. \tag{2.58}
$$

Here, $Q_{\mathrm{eff}} = \max(3\langle Q_{\mathrm{pr}} \rangle, Q_{\mathrm{sw}})$ is the effective cross-section efficiency. For numerical convenience, we approximate Q_{eff} as:

$$
Q_{\mathrm{eff}} = \begin{cases} \frac{2X}{3} & X \leq \frac{9}{2} \\[2ex] 3 & X > \frac{9}{2} \end{cases}. \tag{2.59}
$$

---

[1]Note that $X = 2a/l(p_0)$ in plasma differential PR drag should not be confused with $x = 2\pi a/\lambda$ in photon differential PR drag.
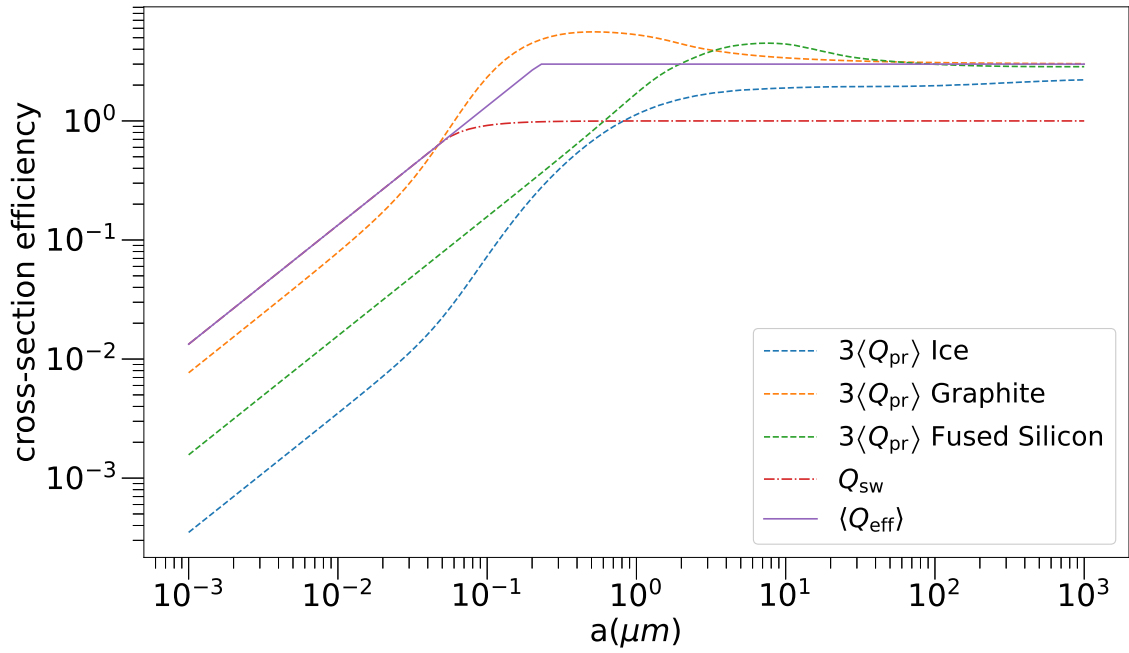
Figure 2.4: Comparison of average pressure cross-section efficiency ($\langle Q_{\mathrm{pr}} \rangle$) of ice, graphite, and fused silicon (dashed line), momentum transfer cross-section efficiency ($\langle Q_{\mathrm{sw}} \rangle$) (dashed dot line), and the approximation value of the cross-section efficiency ($\langle Q_{\mathrm{eff}} \rangle$) (solid line). Pressure cross-section efficiencies are computed using optical constants of ice (Warren & Brandt, 2008), graphite (Djurišić & Li, 1999), and fused silicon (Kitamura et al., 2007).

Figure 2.4 presents a comparison of the average pressure cross-section efficiency of ice, graphite, and fused silicon (dashed line), the momentum transfer cross-section efficiency (dashed dot line), and the approximation of Q_{eff} (solid line). The approximation accurately reproduces Q_{sw} for small grains and $3\langle Q_{\mathrm{pr}} \rangle$ for large grains.

2.9   Trajectory of Dust Grains in a Magnetic Field

To derive the equation of motion for a dust grain with charge Q under the influence of the Lorentz force $\mathbf{F}_B$ in the Parker spiral magnetic field, we begin with:

$$\mathbf{F}_B = \left(\frac{Q}{c}\right) \mathbf{v} \times \mathbf{B}. \tag{2.60}$$

27
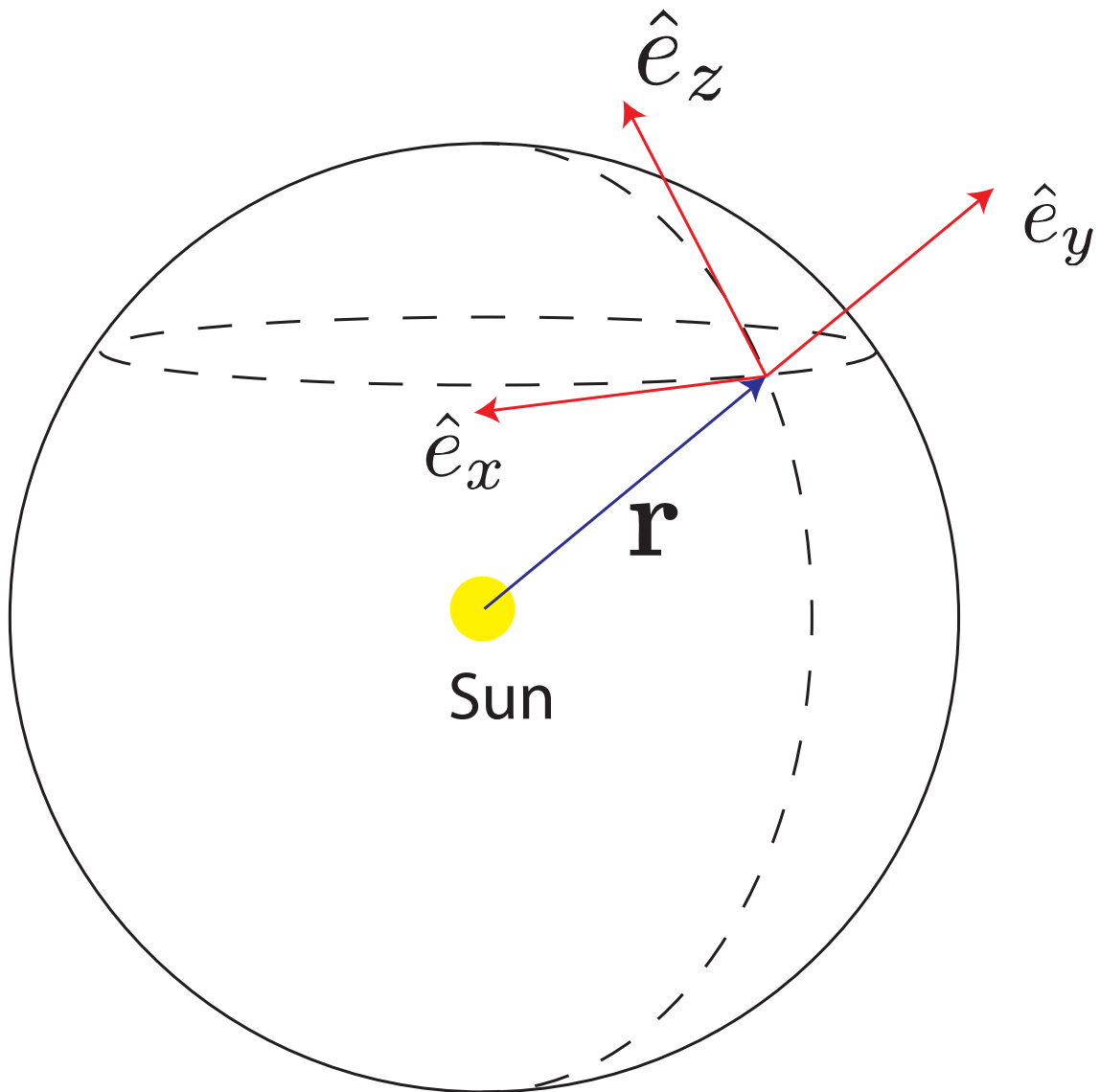
Figure 2.5: Schematic illustration of the local coordinate system defined in the spherical coordinate framework (Lazarian & Hoang, 2007).

We introduce a local orthonormal coordinate system (e_x, e_y, e_z) defined in the spherical coordinate framework, as shown in Fig. 2.5. The local axes are defined as: $e_y = e_r$ (radial direction), $e_z = -e_\theta$ (opposite to the polar direction), and $e_x = e_\phi$ (azimuthal direction), where e_r, e_θ, and e_ϕ are the standard spherical unit vectors.

In this coordinate system, the Parker spiral magnetic field can be expressed as $\mathbf{B} = (B_\phi, B_r, 0)$ (see Appendix 5). Considering a dust grain moving in the ecliptic plane with an unperturbed Keplerian velocity, we express the perturbed position components as:

$$r\phi = r\phi_0 + r\dot{\phi}_0 t + \delta x,$$

$$r\theta = -\delta z,$$

$$r = r_0 + \delta y, \tag{2.61}$$

where ϕ_0, $\dot{\phi}_0$, and r_0 are constants determined by the initial conditions. For Keplerian motion, the angular velocity is $\dot{\phi}_0 = \sqrt{GM_\odot/r_0^3}$. The linearized equations governing the perturbations due to the Lorentz force are:

$$m\delta\ddot{x} = -QB_r\delta\dot{z},$$

$$m\delta\ddot{y} = QB_\phi\delta\dot{z} - \frac{GM_\odot m}{r_0^3}\delta y,$$

$$m\delta\ddot{z} = Q\left(B_r\delta\dot{x} - B_\phi\delta\dot{y}\right) - \frac{GM_\odot m}{r_0^3}\delta z, \tag{2.62}$$

where m is the grain mass and $M_\odot$ is the solar mass.

The general solution for the perturbations can be expressed as:

$$\begin{pmatrix} \delta x \\ \delta y \\ \delta z \end{pmatrix} = \sum_{i=1}^{6} C_i \mathbf{v}_i e^{\lambda_i t}, \tag{2.63}$$

where C_i are constants set by initial conditions, $\mathbf{v}_i$ are the eigenvectors, and λ_i are the eigenvalues obtained from the characteristic equation:

$$\lambda^2 \left(\lambda^4 + \left(\frac{2GM_\odot}{r^3} + \frac{Q^2}{m^2}(B_\phi^2 + B_r^2) \right) \lambda^2 + \left(\frac{GM_\odot}{r^3} \right)^2 + \frac{GM_\odot}{r^3} \frac{Q^2}{m^2} B_r^2 \right) = 0. \tag{2.64}$$

This equation implies that all eigenvalues are either zero or purely imaginary. Consequently, the dust grain undergoes oscillatory motion around the unperturbed Keplerian orbit. This behavior is consistent with the findings of Mukai & Giese (1984), who showed that the Lorentz force induces changes in orbital inclination. The timescale associated with the inclination variation due to the Lorentz force is given by:

$$t_{\mathrm{B}} = 6.8 \times 10^{27} \frac{s^4 \rho^2}{V^2} r \frac{\langle i^2 \rangle}{\cos^2 i} \quad \mathrm{yrs}, \tag{2.65}$$

where V is the grain potential in volts, s is the grain radius in centimeters, ρ is the mass density in $\mathrm{g\,cm^{-3}}$, r is the heliocentric distance in astronomical units (au), and i is the inclination in radians.

2.10 Incorporating Rotational Disruption into Grain Size Distribution Models

Once the timescales for different disruption and replenishment mechanisms are obtained, the size distribution can be computed using the model proposed by Wyatt et al. (2011). In this model, small particles are replenished by the collisional disruption of larger ones, with the replenishment rate determined by a redistribution function. Following their derivation, rotational disruption is included as an additional fragmentation mechanism, assuming that the fraction of grains trapped in a high-J attractor point is $f_{\mathrm{highJ}} = 1$ (Herranen et al., 2021).

Our model makes several key assumptions: (1) spherical grain geometry with uniform composition, (2) steady-state conditions in the dust population, (3) negligible effects from radiation pressure on sub-micron grains, and (4) constant tensile strength throughout the grain volume. While these simplifications enable analytical tractability, we acknowledge they may introduce systematic uncertainties, particularly for highly irregular or compositionally heterogeneous grains.

Consider a belt of particles where m_k represents the total mass in the k-th bin, D_k denotes the typical size of particles in that bin, and the bin width is defined by $D_{k+1}/D_k = 1 - \delta$. This work adopts a bin width of $\delta = 0.002$, satisfying the criterion $\delta \ll 1$ (Wyatt et al., 2011). From mass conservation, the governing equation is:

$$\dot{m}_k = \dot{m}_k^{+\mathrm{c}} - \dot{m}_k^{-\mathrm{c}} + \dot{m}_k^{+\mathrm{r}} - \dot{m}_k^{-\mathrm{r}} - \dot{m}_k^{-\mathrm{pr}}, \tag{2.66}$$

where the subscripts and superscripts denote mass gained or lost due to collisional

disruption (c), rotational disruption (r), and Poynting-Robertson (PR) drag (pr).

Assuming that fragments follow a power-law distribution from sizes $\eta_{\text{rmax}} D_k$ to infinitesimally small particles with a power index α_r, the redistribution function $F_r(k-i)$ describes the fraction of mass leaving the i-th bin and entering the k-th bin (Wyatt et al., 2011):

$$F_r(l) = \eta_{\text{rmax}}^{\alpha_r - 4}(4 - \alpha_r)\delta(1 - \delta)^{l(4-\alpha_r)}. \tag{2.67}$$

Both collisional and rotational disruption are assumed to share the same cascade properties, i.e., η_{rmax} and α_r. The adopted values are $\alpha_r = 3.5$ and $\eta_{\text{rmax}} = 2^{-1/3}$ (Wyatt et al., 2011).

To set boundary conditions, the upper boundary is defined at the bin where the typical particle size is D_1, with the assumption that the total loss rate from fragmentation outside this boundary ($> D_1$) remains constant:

$$\dot{m}_k^{+\text{c}} + \dot{m}_k^{+\text{r}} = \sum_{i=1}^{k-1}(\dot{m}_i^{-\text{c}} + \dot{m}_i^{-\text{r}})F_r(k-i) + \dot{m}_{\text{b}}^{-}\sum_{l=k}^{\infty}F_r(l). \tag{2.68}$$

Here, the second term on the right-hand side represents the mass loss rate $\dot{m}_{\text{b}}^{-}$ beyond the upper boundary, which is assumed constant.

Under the assumption of a quasi-steady-state distribution ($\dot{m}_k = 0$), Equation 2.68 simplifies to:

$$\dot{m}_{ks}^{-\text{c}} + \dot{m}_{ks}^{-\text{r}} + \dot{m}_{ks}^{-\text{pr}} = \sum_{i=1}^{k-1}(\dot{m}_{is}^{-\text{c}} + \dot{m}_{is}^{-\text{r}})F_r(k-i) + \dot{m}_{\text{b}}^{-}\sum_{l=k}^{\infty}F_r(l). \tag{2.69}$$

For consistency with observed dust populations at $1\,\text{au}$, the value $\dot{m}_{\text{b}}^{-} = 900\delta\,\text{g/s} = 1.8\,\text{g/s}$ is chosen, approximately matching the number of particles at $a = 10^2\,\mu\text{m}$

32

when rotational disruption is absent ($R^r = 0$). This estimate is based on the most massive dust population at $\sim 100\,\mu$m (Grün et al., 1985; Love & Brownlee, 1993).

The collisional mass loss rate, $R_k^c = \dot{m}_k^{-c}/m_k$, depends on the dust grain size distribution and follows Wyatt et al. (2011):

$$R_k^c = \sum_{i=1}^{i_{ck}} \frac{3m_i}{2\rho\pi D_i^3}(D_k + D_i)^2 P_{ik}, \qquad (2.70)$$

where P_{ik} is the intrinsic collision probability, given by $P_{ik} = \pi v_{\text{rel}}/V$. The parameter $V = 2\pi^2 e^2 r^3$ represents the volume occupied by the particles, with an average eccentricity $e = 0.3$ (Ipatov et al., 2008). The index i_{ck} corresponds to the bin with size $X_c D_k$, where X_c is given by:

$$X_c = (2Q_D^*/v_{\text{rel}}^2)^{1/3}. \qquad (2.71)$$

Here, $v_{\text{rel}} \simeq e\sqrt{\frac{GM_\odot}{r}} \simeq 9\sqrt{\frac{1\,\text{au}}{r}}$ km/sec, and the dispersal law for Q_D^* is:

$$Q_D^* = Q_b D^{-b} + Q_c D^c, \qquad (2.72)$$

where $Q_b = 790\,\text{J}\,\text{kg}^{-1}$, $b = 0.38$, $Q_c = 0.017\,\text{J}\,\text{kg}^{-1}$, and $c = 1.36$, with D in meters.

The mass loss rates for rotational disruption ($R_k^r = \dot{m}_k^{-r}/m_k$) and PR drag ($R_k^{-\text{pr}} = \dot{m}_k^{-\text{pr}}/m_k$) are inversely proportional to the disruption timescales t_{disr} (Equation 2.36) and t_{PR} (Equation 2.53), respectively. The size distribution is then obtained by solving:

$$m_k = \frac{\dot{m}_k^{-c} + \dot{m}_k^{-r} + \dot{m}_k^{-\text{pr}}}{R_k^c + R_k^r + R_k^{-\text{pr}}} = \frac{\dot{m}_k^{-c} + \dot{m}_k^{-r} + \dot{m}_k^{-\text{pr}}}{\tau_{\text{c},k}^{-1} + t_{\text{disr},k}^{-1} + t_{\text{PR},k}^{-1}}. \qquad (2.73)$$

33
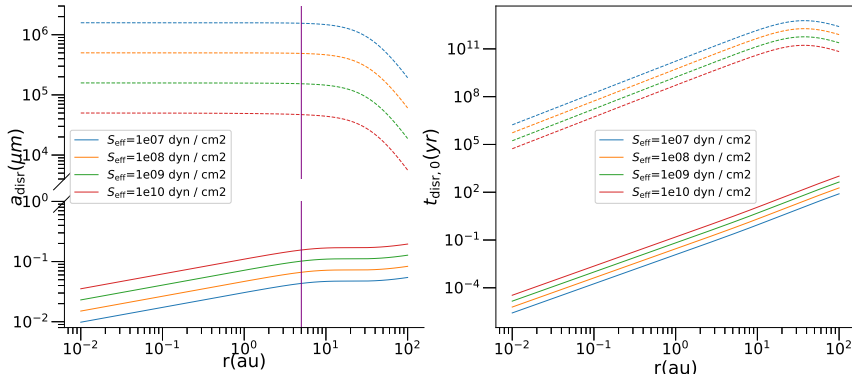
Figure 2.6: Grain disruption properties as a function of heliocentric distance. Left panel: Disruption grain size (a_{disr}) versus heliocentric distance (r) for different effective tensile strengths (S_{eff}). The upper curves represent maximum disruption sizes (Equations 2.34), while lower curves show minimum disruption sizes (Equations 2.32). This reveals the size range of grains susceptible to RATD at each distance. Right panel: Characteristic disruption timescales evaluated at $a = a_{\text{disr}}$, demonstrating how quickly grains of various tensile strengths will fragment. The vertical purple line at $5 \, \text{au}$ marks the conventional water snow line temperature boundary ($170 \, \text{K}$), highlighting how RATD mechanisms extend beyond traditional thermal constraints for dust evolution.

This equation is solved iteratively to determine the steady-state size distribution. Section 3.3 presents a comparison between the numerical results for cases with and without rotational disruption.

Since the size distribution is influenced by different disruption mechanisms, variations in these models yield different results. Additionally, the model does not account for radiation pressure, which expels micrometer-sized particles, nor does it consider the Lorentz force on sub-micron grains.

2.11   Modeling the Distribution of Dust Grains in high-J and low-J Attractor Points

In Section 2.10, we assumed that dust grains are always trapped at a high-J attractor point. However, RATD cannot be so efficient. If grains subject to only

radiative torques, i.e., disregarding magnetic torques, Lazarian & Hoang (2007) showed that the parameter space of a grain can include scenarios where there are no high-J attractor points, and Herranen et al. (2021) demonstrated that the fraction of grains trapped in a high-J attractor point f_{highJ} is always lower than 1 in their ensemble of grain shapes. However, for grains with embedded iron inclusions, the value of f_{highJ} can reach 100% due to the effect of enhanced magnetic relaxation (Herranen et al., 2021; Hoang & Lazarian, 2016). Note that only grains at high-J attractors can be disrupted by RATD. In Appendix 5, we estimate magnetic torques on heliospheric dust, and suggest that they could significantly vary f_{highJ} depending on dust size, charge distribution, and magnetic properties.

To keep things simple, unless otherwise stated, we consider f_{highJ} as a free parameter and adopt a fixed fraction f_{highJ} for all fragment sizes originating from the border and various fragmentation methods. Let $m_{\text{H},k}$ and $m_{\text{L},k}$ represent the mass of the dust grains trapped in a high-J attractor point and a low-J attractor point in the k-th bin, respectively. With reference to Equation 2.69, the following are the loss rate equations for $m_{\text{H},k}$ and $m_{\text{L},k}$:

For grains in a high-J attractor point:

$$\dot{m}_{\text{H},ks}^{-\text{c}} + \dot{m}_{\text{H},ks}^{-\text{r}} + \dot{m}_{\text{H},ks}^{-\text{pr}} = f_{\text{highJ}} \sum_{i=1}^{k-1} (\dot{m}_{is}^{-\text{c}} + \dot{m}_{\text{H},is}^{-\text{r}}) F_r(k-i) + f_{\text{highJ}} \dot{m}_{\text{b}}^{-} \sum_{l=k}^{\infty} F_r(l). \qquad (2.74)$$

For grains in a low-J attractor point:

$$\dot{m}_{\text{L},ks}^{-\text{c}} + \dot{m}_{\text{L},ks}^{-\text{pr}} = (1 - f_{\text{highJ}}) \sum_{i=1}^{k-1} (\dot{m}_{is}^{-\text{c}} + \dot{m}_{\text{H},is}^{-\text{r}}) F_r(k-i) + (1 - f_{\text{highJ}}) \dot{m}_{\text{b}}^{-} \sum_{l=k}^{\infty} F_r(l). \qquad (2.75)$$

The size distribution of grains trapped in high-*J* and low-*J* attractor points can be obtained by solving the following equations for $m_{\mathrm{H},k}$ and $m_{\mathrm{L},k}$:

For grains in a high-*J* attractor point:

$$m_{\mathrm{H},k} = \frac{\dot{m}_{H,k}^{-\mathrm{c}} + \dot{m}_{H,k}^{-\mathrm{r}} + \dot{m}_{H,k}^{-\mathrm{pr}}}{\tau_{\mathrm{c},k}^{-1} + t_{\mathrm{disr},k}^{-1} + t_{\mathrm{PR},k}^{-1}}. \tag{2.76}$$

For grains in a low-*J* attractor point:

$$m_{\mathrm{L},k} = \frac{\dot{m}_{L,k}^{-\mathrm{c}} + \dot{m}_{L,k}^{-\mathrm{pr}}}{\tau_{\mathrm{c},k}^{-1} + t_{\mathrm{PR},k}^{-1}}. \tag{2.77}$$

And the total size distribution is the following:

$$m_k = m_{\mathrm{H},k} + m_{\mathrm{L},k}. \tag{2.78}$$

Therefore, the mass loss rate due to collisions R_k^c is given by:

$$R_k^c = \sum_{i=1}^{i_{ck}} \frac{3m_i}{2\rho\pi D_i^3}(D_k + D_i)^2 P_{ik} = \sum_{i=1}^{i_{ck}} \frac{3(m_{\mathrm{H},i} + m_{\mathrm{L},i})}{2\rho\pi D_i^3}(D_k + D_i)^2 P_{ik}. \tag{2.79}$$

2.12 Incorporating the Lorentz Effect into Grain Size Distribution Models

Following the framework established in Section 2.11, the Lorentz force can be incorporated into the grain size distribution model. For grains located at a high-*J* attractor point, the mass loss equation becomes:

36
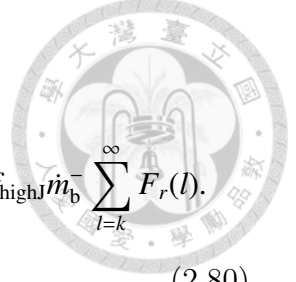
$$\dot{m}_{\mathrm{H},ks}^{-c} + \dot{m}_{\mathrm{H},ks}^{-r} + \dot{m}_{\mathrm{H},ks}^{-pr} + \dot{m}_{\mathrm{H},ks}^{-B} = f_{\mathrm{highJ}} \sum_{i=1}^{k-1} \left(\dot{m}_{is}^{-c} + \dot{m}_{\mathrm{H},is}^{-r} \right) F_r(k-i) + f_{\mathrm{highJ}} \dot{m}_{\mathrm{b}}^{-} \sum_{l=k}^{\infty} F_r(l).$$

(2.80)

For grains located at a low-J attractor point, the corresponding equation is:

$$\dot{m}_{\mathrm{L},ks}^{-c} + \dot{m}_{\mathrm{L},ks}^{-pr} + \dot{m}_{\mathrm{L},ks}^{-B} = (1 - f_{\mathrm{highJ}}) \sum_{i=1}^{k-1} \left(\dot{m}_{is}^{-c} + \dot{m}_{\mathrm{H},is}^{-r} \right) F_r(k-i) + (1 - f_{\mathrm{highJ}}) \dot{m}_{\mathrm{b}}^{-} \sum_{l=k}^{\infty} F_r(l).$$

(2.81)

Here, the superscript "$-B$" denotes the mass loss due to the Lorentz force, and the other superscripts refer to losses from collisions ($-c$), radiative torques ($-r$), and Poynting-Robertson drag ($-pr$).

The mass of grains at the high-J attractor point can be expressed as:

$$m_{\mathrm{H},k} = \frac{\dot{m}_{\mathrm{H},k}^{-c} + \dot{m}_{\mathrm{H},k}^{-r} + \dot{m}_{\mathrm{H},k}^{-pr} + \dot{m}_{\mathrm{H},k}^{-B}}{\tau_{\mathrm{c},k}^{-1} + t_{\mathrm{disr},k}^{-1} + t_{\mathrm{PR},k}^{-1} + t_{\mathrm{B},k}^{-1}},$$

(2.82)

while for grains at the low-J attractor point:

$$m_{\mathrm{L},k} = \frac{\dot{m}_{\mathrm{L},k}^{-c} + \dot{m}_{\mathrm{L},k}^{-pr} + \dot{m}_{\mathrm{L},k}^{-B}}{\tau_{\mathrm{c},k}^{-1} + t_{\mathrm{PR},k}^{-1} + t_{\mathrm{B},k}^{-1}}.$$

(2.83)

The total mass at grain size bin k is then given by the sum of both components:

$$m_k = m_{H,k} + m_{L,k}.\qquad(2.84)$$

Finally, the mass loss rate due to collisions, R_k^c, is calculated as:

$$R_k^c = \sum_{i=1}^{i_{ck}} \frac{3(m_{H,i} + m_{L,i})}{2\rho\pi D_i^3}(D_k + D_i)^2 P_{ik},\qquad(2.85)$$

where D_i and D_k are the grain diameters in size bins i and k, respectively, ρ is the grain material density, and P_{ik} is the collision probability between grains in bins i and k.

Chapter 3   Numerical Results

In this section, we present the numerical results of the Radiative Torque Disruption (RATD) theory applied to the Solar System. This includes the disruption sizes and characteristic timescales for various fragmentation mechanisms and different fractions of grain alignment. We also examine how the positions of the present water snow line shift with different grain sizes due to RATD effects in the Solar System. The computational domain for this analysis spans from $10^{-3}\,\mu\mathrm{m}$ to $D_1 = 10^4\,\mu\mathrm{m}$, with the total mass of the bins outside the lower boundary extrapolated from the values within this range. Since the observed dust size distribution described in Equation 2.11 was obtained at $1\,\mathrm{au}$, we focus on a heliocentric distance of $1\,\mathrm{au}$ as the fiducial location to study the effect of RATD on the dust size distribution in Sections 3.2 and 3.3. Additionally, we discuss the effect of radiation pressure, which is not included in our model, on dust grains affected by RAT in the heliosphere.

3.1   Disruption Sizes and Characteristic Times of Dust Grains

Figure 2.6 presents the minimum and maximum grain disruption sizes and their corresponding RATD timescales, as discussed in Section 2.5. The left panel shows that the disruption size of dust grains ranges from approximately $0.01\,\mu\mathrm{m}$ to $0.1\,\mu\mathrm{m}$.
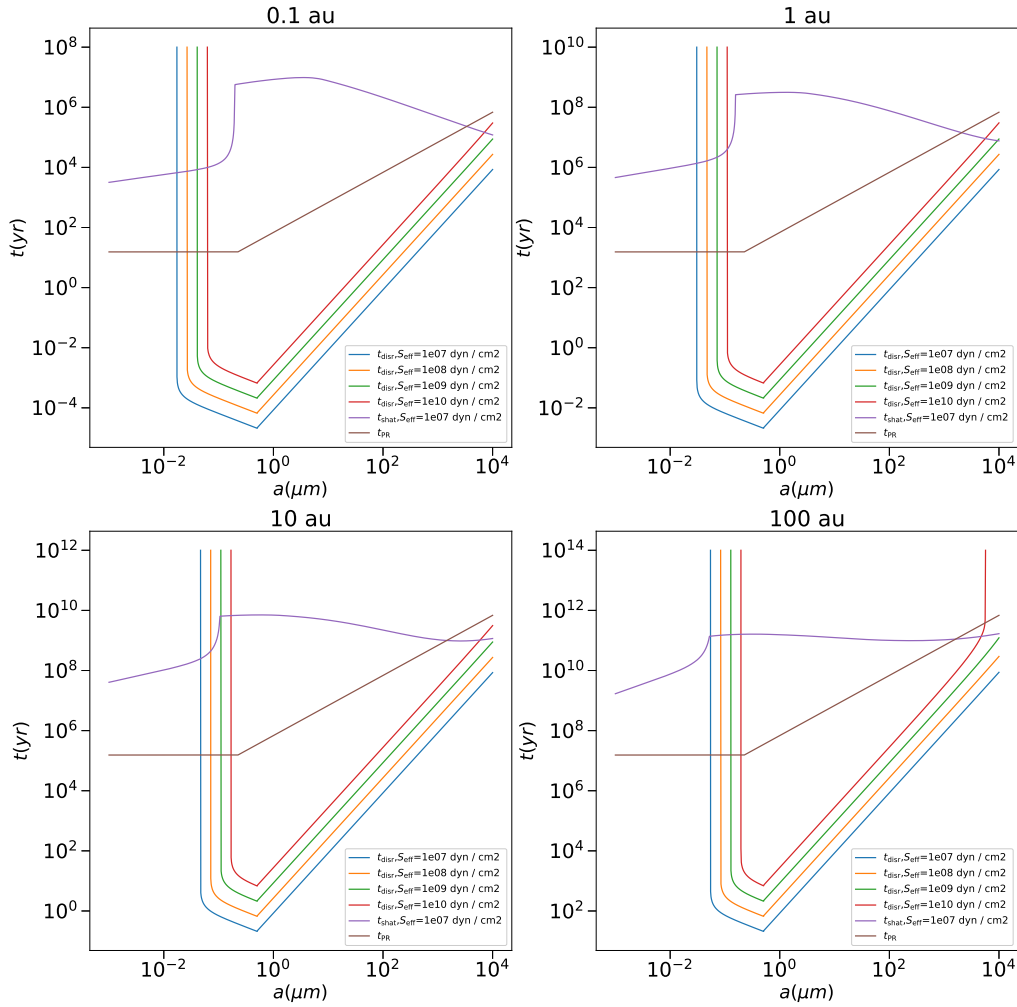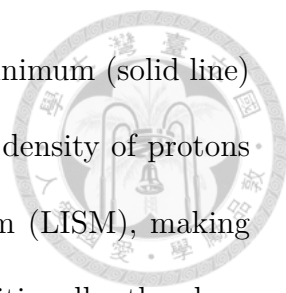
Figure 3.1: The characteristic times of different mechanisms of fragmentation and tensile strengths, S_{eff}, as a function of grain size at heliocentric distances of $0.1\,\text{au}$, $1\,\text{au}$, $10\,\text{au}$, and $100\,\text{au}$. The vertical curves arise because the timescale of rotational disruption diverges at $a_{\text{disr,min}}$ and $a_{\text{disr,max}}$. The plotted timescales include those for rotational disruption (t_{disr}), PR drag (t_{PR}), and collisional disruption (t_{shat}).

The disruption range is defined by the grain sizes between the minimum (solid line) and maximum (dashed line) disruption sizes. For $r > 10\,\mathrm{au}$, the density of protons in the solar wind is lower than in the Local Interstellar Medium (LISM), making the disruption size predominantly influenced by the LISM. Additionally, the slope of the minimum and maximum disruption size curves, $a_{\mathrm{disr,min}}$ and $a_{\mathrm{disr,max}}$, changes slightly beyond $10\,\mathrm{au}$. The minimum disruption size shifts due to the lower drift velocity of protons in the LISM, which reduces $K(s)$ in Equation 2.32. The maximum disruption size, on the other hand, changes more significantly because the proton density transitions from $n_{\mathrm{H}} \propto r^{-2}$ to a constant (see Equation 2.34). Interestingly, the maximum disruption size can reach up to $1\,\mathrm{m}$. However, such large grains would take an extended period to be disrupted and are more likely to be destroyed by grain-grain collisions first (see Fig. 3.1). For grain sizes smaller than $a_{\mathrm{disr,min}}$, since they cannot be disrupted by RATD, PR drag will remove them on the timescale t_{PR}.

To illustrate the significance of rotational disruption, we compare the characteristic timescales of rotational disruption (Equation 2.36), PR drag (Equation 2.53), and collisional disruption (Equation 2.85) as functions of grain size at different heliocentric distances in Fig. 3.1. The collisional disruption timescales are computed using the size distribution obtained in Section 2.11 with $S_{\mathrm{eff}} = 10^{7}\mathrm{dyn\ cm}^{-2}$ and $f_{\mathrm{highJ}} = 0.8$. The results indicate that the overall trends are similar for $r < 100\,\mathrm{au}$. As expected, the timescale of rotational disruption diverges at $a_{\mathrm{disr,min}}$ and $a_{\mathrm{disr,max}}$, as described in Equations 2.32 and 2.34. The rotational disruption timescale is shortest for grain sizes between $a_{\mathrm{disr,min}}$ and $10^{4}\,\mu\mathrm{m}$. Furthermore, all characteristic timescales increase as the heliocentric distance r increases. A noticeable change in slope occurs at $a = 0.51\,\mu\mathrm{m}$ for the rotational disruption timescale, due to a reduction in Ra-

diative Torque (RAT) efficiency in Equation 2.17. Additionally, there is a sudden change in the collisional disruption timescale at dust size a, where $X_c(a)a = a_{\mathrm{disr,min}}$. This abrupt change arises from variations in mass distribution included in the summation in Equation 2.70.

It is important to note that Fig. 3.1 shows that the collisional timescale becomes larger than the PR timescale for dust sizes $< 10^3 \, \mu$m. This is a consequence of our choice of boundary condition ($\dot{m}_{\mathfrak{b}}^-$), which roughly captures the most massive dust population of $100 \, \mu$m at $1 \, \mathrm{au}$. In the absence of RATD, the dust size evolution transitions from a collision-dominated regime for larger sizes ($> \sim 100 \, \mu$m) to a PR-drag-dominated regime for smaller sizes ($< \sim 100 \, \mu$m), which aligns with theoretical predictions (e.g., Grün et al., 1985).

Key Findings: Our analysis reveals that RATD is most efficient for dust grains between $0.1 \, \mu$m and $100 \, \mu$m throughout the heliosphere ($r < 100 \, \mathrm{au}$), with characteristic disruption timescales significantly shorter than competing mechanisms for grains trapped in high-J attractors. The efficiency zone for RATD extends beyond the conventional water snow line ($\sim 5 \, \mathrm{au}$), suggesting this mechanism substantially modifies dust populations throughout the inner and middle heliosphere. Importantly, the transition from solar wind to LISM gas properties beyond $10 \, \mathrm{au}$ alters disruption size boundaries but maintains RATD's dominance as a fragmentation mechanism.

3.2 Effect of the Fraction of Grain Alignment on Grain Size Distribution

To account for the variation in grain alignment at high-J attractors with respect to grain size, charge, shape, and magnetic properties (Herranen et al., 2021; Hoang & Lazarian, 2016) (also see Appendix 5), we vary the fraction f_{highJ} from 0 to 1. Figure 3.2 presents the mass distribution for different values of f_{highJ} with a tensile strength of $S_{\text{eff}} = 10^7 \text{dyn cm}^{-2}$ and a mass loss rate of $\dot{m}_{\text{b}}^{-} = 1.8\,\text{g/s}$ at 1 au. The results show that the mass distribution falls between the two limiting cases of $f_{\text{highJ}} = 0$ and $f_{\text{highJ}} = 1$.

The impact of RATD on the grain size distribution is highly sensitive to the fraction of grains aligned at high-J attractor points. As f_{highJ} increases, the mass of larger grains ($a > a_{\text{disr,min}}$) decreases due to more efficient rotational disruption, while the relative abundance of smaller grains ($a < a_{\text{disr,min}}$) increases as these fragments accumulate. For the case of $f_{\text{highJ}} = 1$, the mass distribution of large grains is reduced while that of nanodust grains is increased by several orders of magnitude. When $1 > f_{\text{highJ}} > 0.5 - 0.8$, the modification in the mass distribution is weaker but still significant. This demonstrates the high efficiency of RATD in removing large grains under conditions of maximal alignment.

Additionally, Fig. 3.2 reveals a saturation in the mass distribution within the size range $10^2\,\mu\text{m}$ to $10^3\,\mu\text{m}$ for all cases except $f_{\text{highJ}} = 1$. This saturation results from a transition between a PR-drag-dominated regime and a collision-dominated regime for grains trapped in low-J attractor points. In these regimes, the characteristic

43
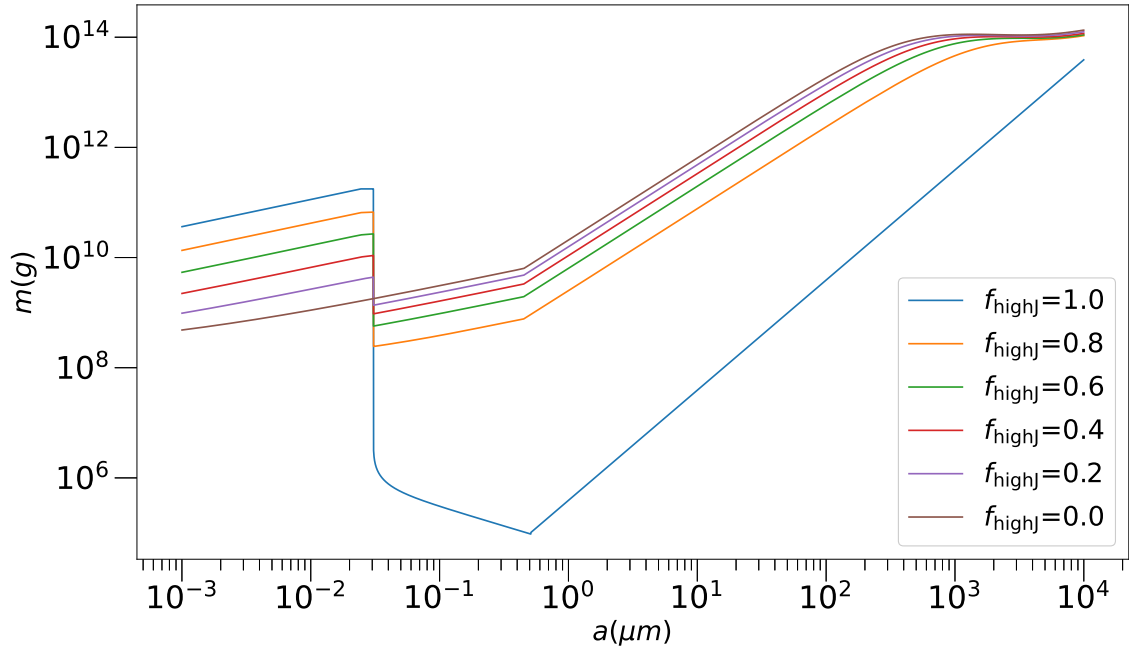
Figure 3.2: Mass distribution of dust grains for different fractions of grain alignment (f_{highJ}) and tensile strength ($S_{\text{eff}} = 10^7 \text{dyn cm}^{-2}$). The mass distribution lies between the cases of $f_{\text{highJ}} = 0$ and $f_{\text{highJ}} = 1$ at $1\,\text{au}$. The y-axis represents the total mass (m) in logarithmic bins centered on grain sizes (a) given on the x-axis.

timescale changes from decreasing with grain size to increasing with grain size (see Fig. 3.1).

3.3   Effect of the Tensile Strength on Size Distribution

We now examine how different tensile strengths in RATD affect the steady-state size distribution. Following the methodology outlined in Section 3.2, we set $D_1 = 10^4\,\mu\text{m}$ and $\dot{m}_{\text{b}}^- = 1.8\,\text{g/s}$ for our fiducial location at $1\,\text{au}$, with a high-J fraction of $f_{\text{highJ}} = 0.8$.

Based on Equation 2.11, the number of particles observed within a size range between D_k and D_{k+1} can be expressed as:

$$N_k = -\frac{\partial F(m, r)}{\partial m}\frac{dm}{dD}\frac{V D_k \delta}{v_k} = -\frac{\partial F(m, r)}{\partial m}\frac{\pi}{2}D_k^3\frac{V\rho\delta}{v_k}, \qquad (3.1)$$
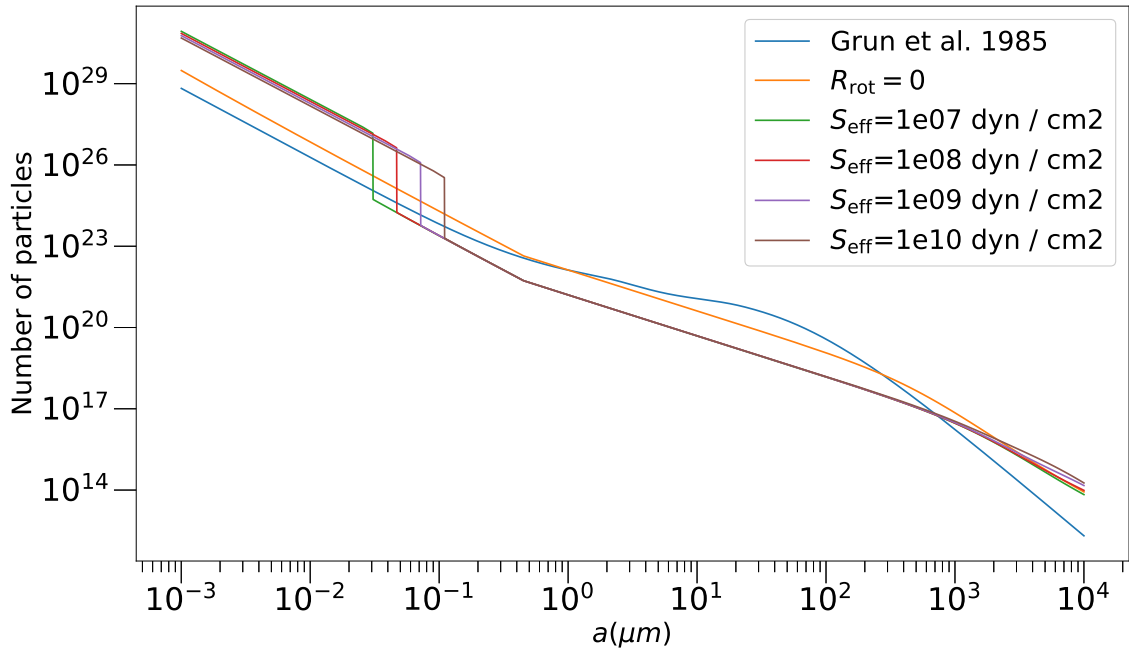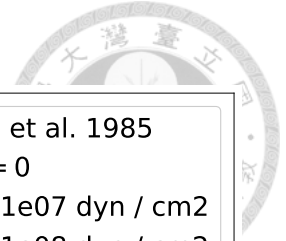
Figure 3.3: The number of particles in each bin at $1\,\mathrm{au}$, with different tensile strengths (S_{eff}) as defined in Section 2.10. The size distribution without rotational disruption, denoted by $R_{\mathrm{rot}} = 0$, is also plotted. The measurement curve at $1\,\mathrm{au}$ provided by Grün et al. (1985) is shown for comparison.
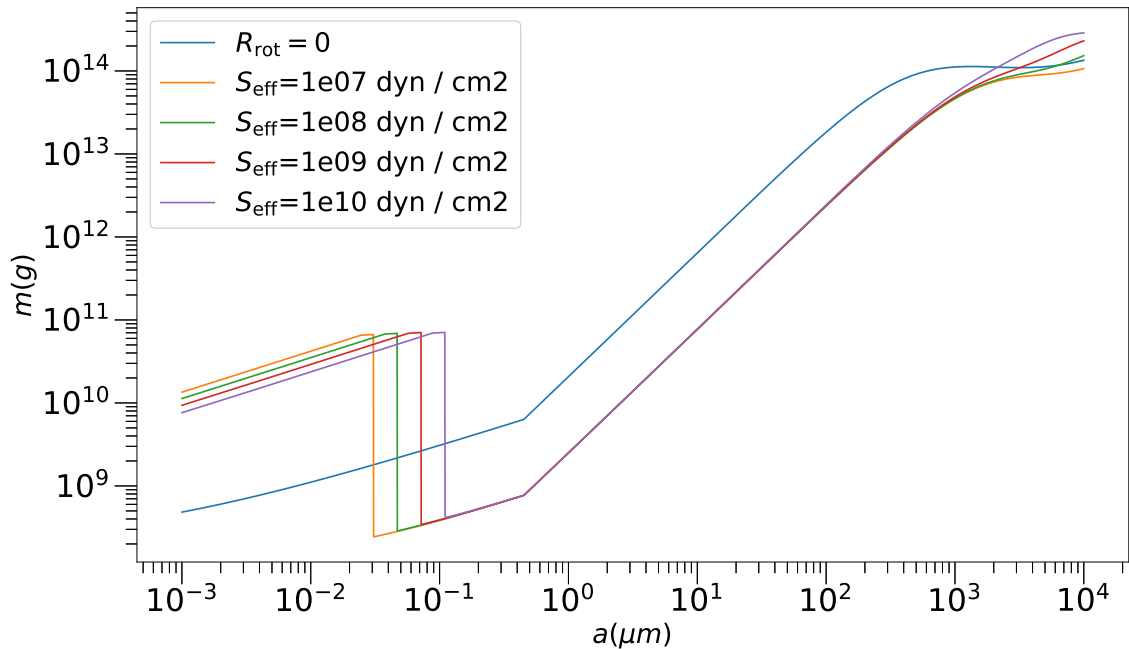
Figure 3.4: The steady-state grain size distribution for different tensile strengths (S_{eff}) with and without rotational disruption at $1\,\mathrm{au}$. The y-axis represents the mass (m) in logarithmic bins centered on grain sizes (a) given on the x-axis. The case $R_{\mathrm{rot}} = 0$ corresponds to the scenario without rotational disruption.
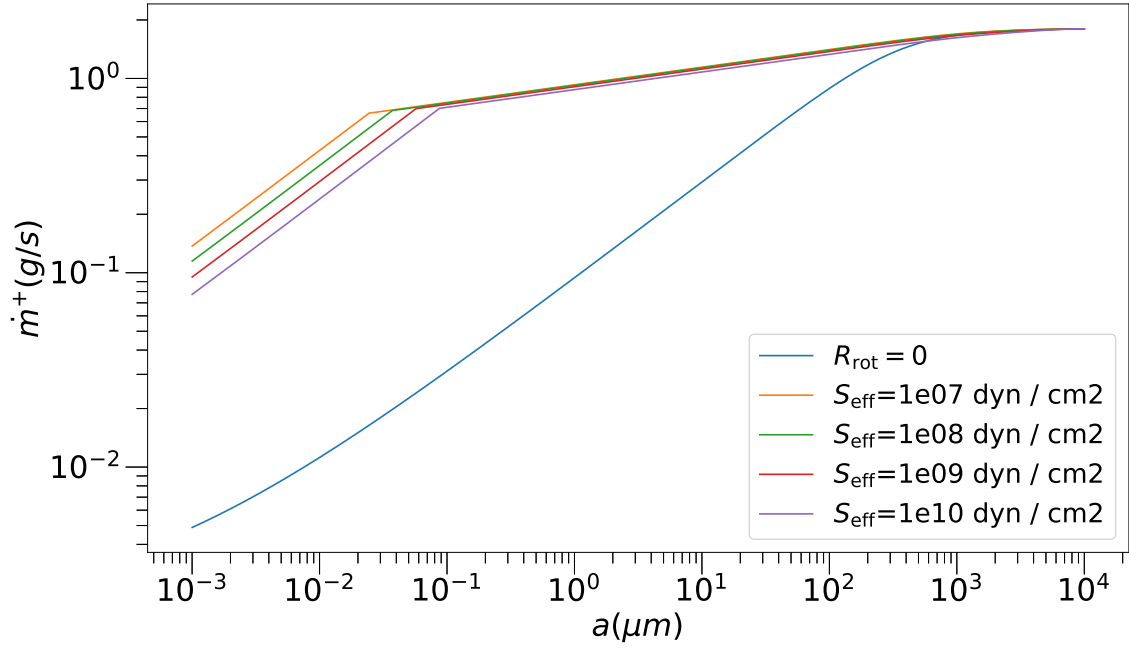
Figure 3.5: The total mass gained as a function of bin size for different tensile strengths (S_{eff}) with and without rotational disruption at $1\,\mathrm{au}$ ($R_{\mathrm{rot}} = 0$ represents no rotational disruption). The y-axis represents the total mass gained ($\dot{m}^+$) in logarithmic bins centered on grain sizes (a) given on the x-axis.
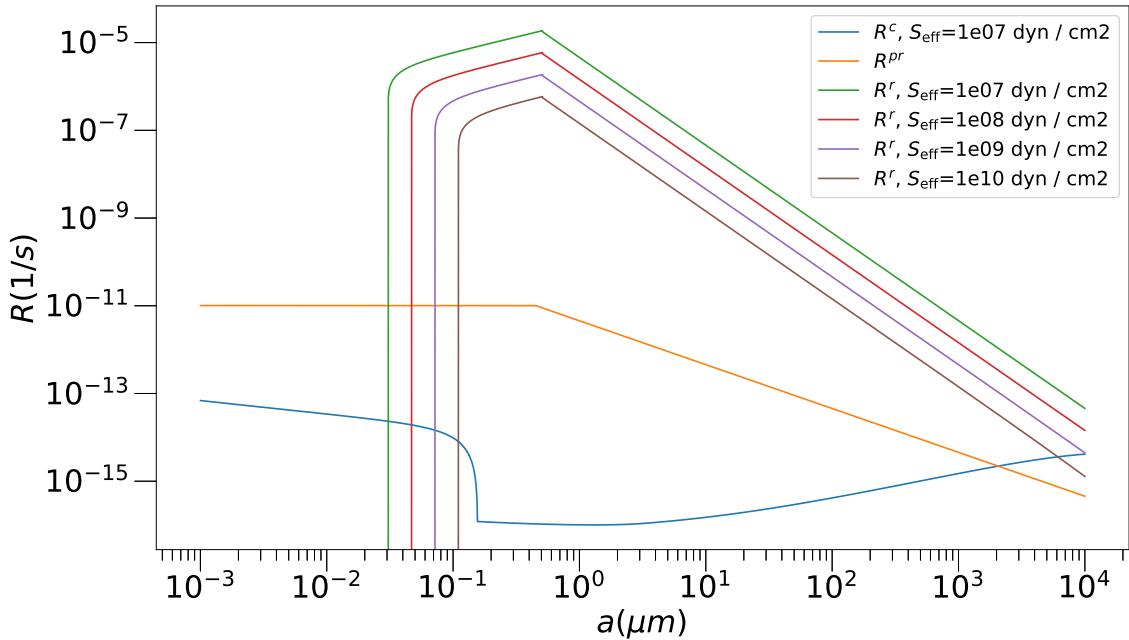
Figure 3.6: The loss rates due to collisions (R^c), rotational disruption (R^r), and PR drag ($R^{-\mathrm{pr}}$) for different bin sizes and tensile strengths (S_{eff}). The y-axis represents the loss rate (R) in logarithmic bins, with the bin centers corresponding to the grain sizes (a) indicated on the x-axis.

where $v_k = \sqrt{\frac{GM_\odot}{r}}$ represents the Keplerian velocity at the heliocentric distance r.

Figure 3.3 illustrates the number of particles in each bin based on numerical results, both with and without considering rotational disruption at $1\,\mathrm{au}$, along with the observational results derived from Equation 3.1 at $1\,\mathrm{au}$. The figure shows that RATD depletes the number of larger dust particles ($> 0.1\,\mu\mathrm{m}$) more efficiently compared to the scenario without RATD. Consequently, the number of smaller dust particles ($< 0.1\,\mu\mathrm{m}$) increases significantly due to rotational fragmentation. This abundance jump of sub-micrometer-sized particles occurs at smaller a for weaker dust tensile strength S_{eff}, as illustrated in Fig. 3.3. This trend is consistent with the results shown in Fig. 3.1.

Figure 3.4 presents the steady-state size (or mass) distribution at $1\,\mathrm{au}$ for different tensile strengths, along with the steady-state size distribution in the absence of rotational disruption. The y-axis represents the mass in logarithmic bins centered on the sizes given on the x-axis. As expected, the mass in micrometer-sized bins is significantly lower when rotational disruption is considered, compared to the size distribution without rotational disruption.

To better understand why the mass in the sub-micrometer size bins is significantly higher when rotational disruption is considered, we plot the total mass gain rate $\dot{m}_k^+ = \dot{m}_k^{+\mathrm{c}} + \dot{m}_k^{+\mathrm{r}}$ in Fig. 3.5 and the loss rates of different mechanisms for varying tensile strengths S_{eff} in Fig. 3.6. These figures indicate that the total mass gain rate for the case without rotational disruption ($R_{\mathrm{rot}} = 0$) decreases more rapidly than cases where RATD is active, particularly in the regime where PR drag dominates over collisions. Therefore, when rotational disruption is absent and collisional frag-

47

mentation is less efficient, the total mass gain rate is significantly lower (i.e., the blue curve in Fig. 3.5) due to the predominant mass loss via PR drag (i.e., the orange curve in Fig. 3.6).

By comparing Fig. 3.4 with Fig. 3.2, we observe that for cases where $f_{\mathsf{highJ}} < 1$, the mass within the size range of $1\,\mu\mathrm{m}$ to $10^3\,\mu\mathrm{m}$ shows no noticeable variation across different values of S_{eff}. This is because, in this size range, the mass is primarily contributed by grains trapped in low-J attractor points. As a result, the distribution in this regime is more sensitive to the alignment fraction f_{highJ} than to the tensile strength of the grains.

3.4 Timescale and Size Distribution Including the Lorentz Effect

Figure 3.7, analogous to Fig. 3.1, presents the characteristic timescales of various dust removal mechanisms, now incorporating the Lorentz effect. The inclusion of the Lorentz timescale t_B shows that for sub-micron (μm-sized) dust grains, the Lorentz force becomes the dominant removal mechanism. This underscores the important role of electromagnetic interactions in regulating the dynamics of small grains in the heliosphere.

Furthermore, the characteristic timescale for collisions becomes longer when the Lorentz effect is included. This is due to the efficient removal of small grains by the Lorentz force, which reduces the grain population and consequently lowers the probability of collisions.

48
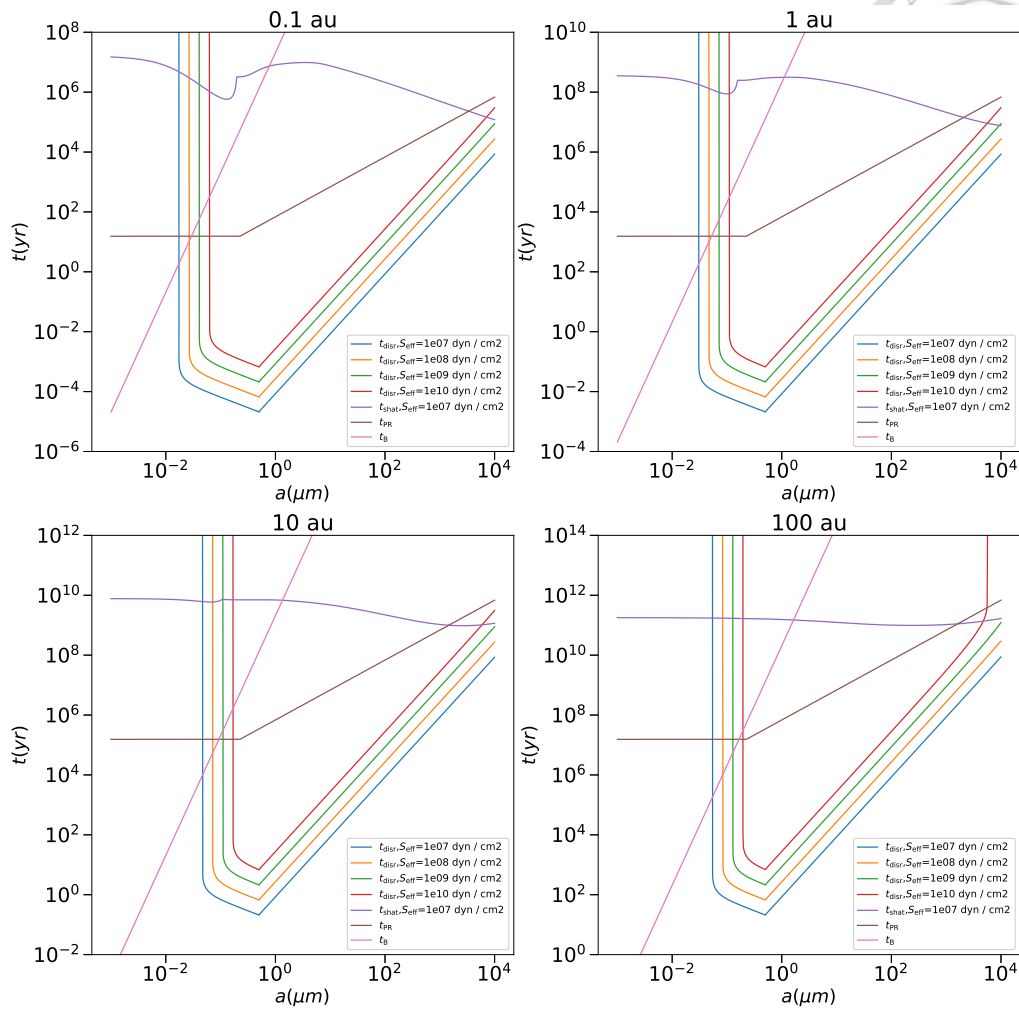
Figure 3.7: Same as Fig. 3.1, but with the inclusion of the Lorentz timescale t_B.
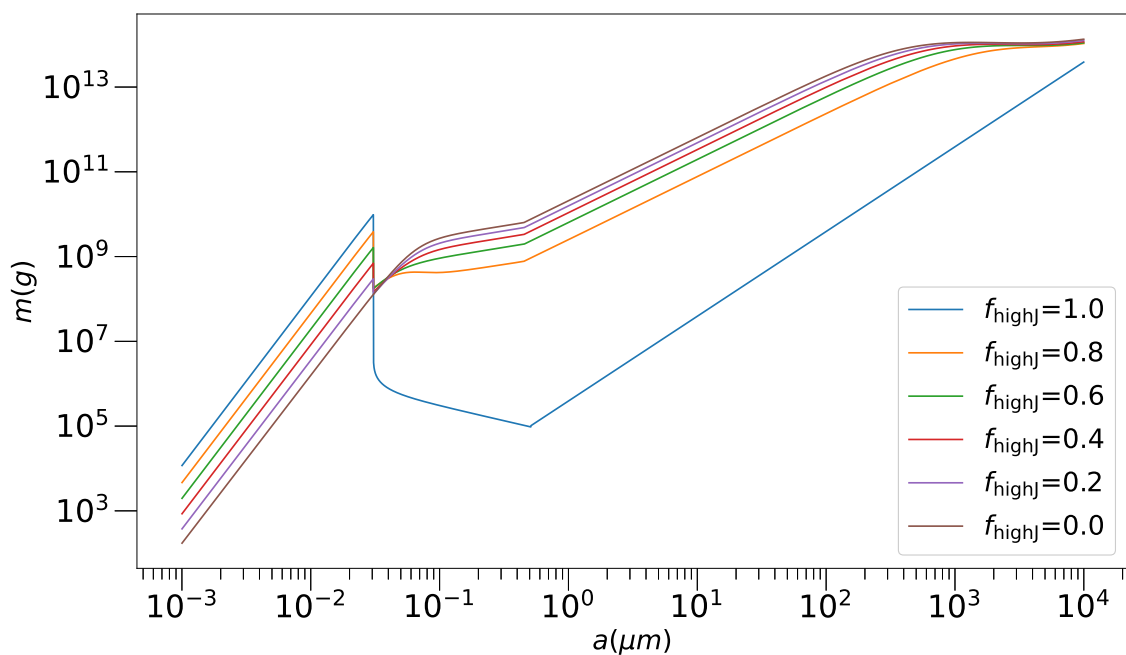
Figure 3.8: Same as Fig. 3.2, but with the Lorentz effect included.
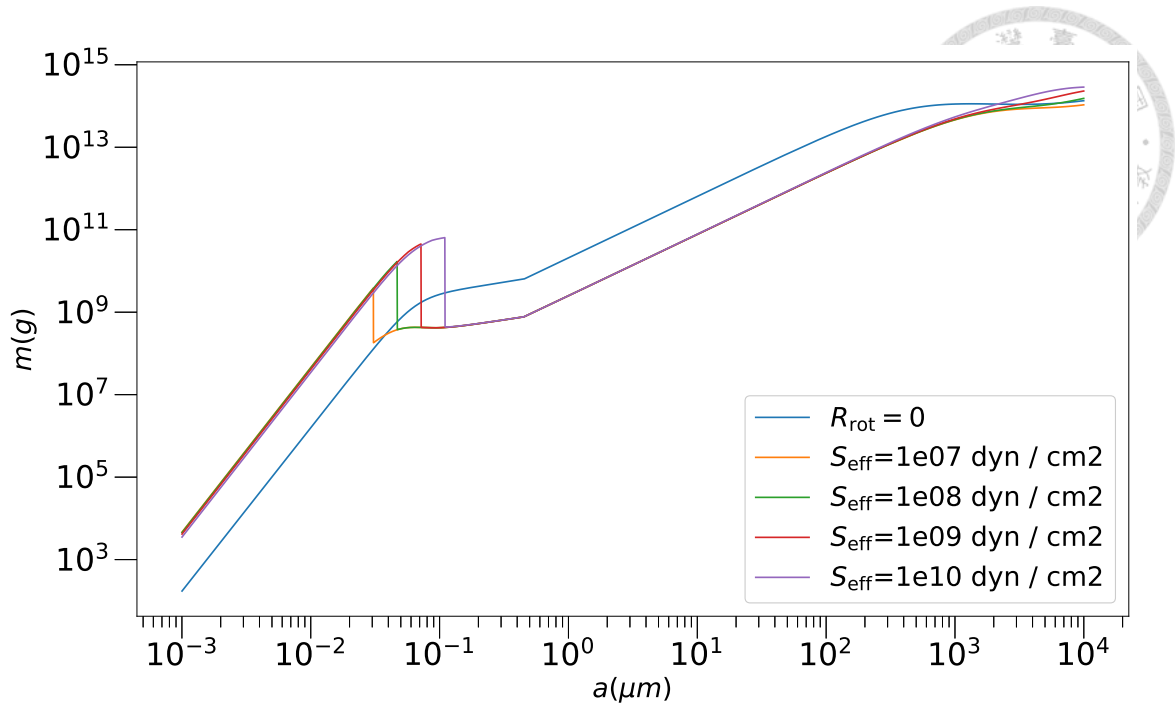
Figure 3.9: Same as Fig. 3.4, but with the Lorentz effect included.

Figures 3.8 and 3.9, analogous to Figs. 3.2 and 3.4, show the resulting grain size distributions when the Lorentz effect is considered. The distributions are shown as functions of the high-J fraction and tensile strength. Compared to the case without the Lorentz effect, the mass of sub-micron grains is significantly reduced. This depletion results from the more rapid removal of small, charged grains via the Lorentz force.

3.5 Water Snow Line of the Present Solar System

Icy grains are particularly interesting as they indicate the location of the snow line. Observations suggest that C-type asteroids, which are one of the primary sources of water-rich chondrites, are located around 2.7 au (Morbidelli et al., 2000). However, there is little direct evidence for the existence of surface ice on asteroids in the main belt (Bockelee-Morvan, 2015), despite the presence of main-belt comets

with uncertain compositions (Hsieh & Jewitt, 2006). Another major source of icy grains in the inner Solar System is comets (e.g., Mann, 2017). Nesvornỳ et al. (2010) found that a significant fraction of the zodiacal cloud originates from the disruption of Jupiter-family comets.

Min et al. (2011) demonstrated that the water snow line in the protosolar nebula is highly sensitive to model parameters and cannot be precisely determined theoretically. Additionally, the effects of planetesimal formation on the asteroid belt remain poorly understood (DeMeo & Carry, 2014; Podolak & Zucker, 2004). As a result, the exact location of the present water snow line is still debated. It is generally defined as the region where the average temperature falls below $170\,\mathrm{K}$, allowing ice grains to condense, which is thought to be around $5\,\mathrm{au}$ (Bockelee-Morvan, 2015; Henin, 2018; Prockter, 2005). However, for a composite grain with an ice mantle and an effective tensile strength S_eff, the present water snow line is also determined by the disruption grain size.

In Fig. 2.6, the vertical line marks the present water snow line, located at $5\,\mathrm{au}$. The disruption grain size can be determined by substituting the parameter values at $5\,\mathrm{au}$ into Equation 2.32 and replacing S_max with S_eff:

$$a_\mathrm{disr,min} \simeq 0.0928 \times S_\mathrm{eff,9}^{1/5.4}\ \mu\mathrm{m}. \tag{3.2}$$

For a given effective tensile strength, which depends on the internal structure of dust grains and the thickness of the ice mantle, as described in Section 2.7, it is evident from the left panel of Fig. 2.6 that larger grains are disrupted by RAT at distances beyond the present water snow line at $5\,\mathrm{au}$. Consequently, the number

density of icy grains inside the present water snow line, as defined by RATD, is significantly lower than the number density of icy grains beyond the present water snow line, as shown in Section 3.3. This implies that for sufficiently large grains, the effective snow line may extend beyond the snow line defined by the sublimation temperature of water ice.

3.6 Effects of Radiation Pressure on Particle Disruption

In previous sections, the RATD effect was analyzed under the assumption that dust grains are on circular orbits and spun up by radiative torques. In this section, we examine the impact of radiation pressure on grain motion and the implications for the RATD effect.

Radiation pressure plays a crucial role in stellar winds and dust grain dynamics. For Solar-type and late-type stars, Minato et al. (2006) demonstrated that stellar wind pressure remains ineffective unless $\dot{M} > 10^3 \dot{M}_\odot$. Conversely, in early-type stars, stellar winds are primarily governed by line-driven winds, wherein radiation transfers momentum to wind elements via absorption in spectral lines (Castor et al., 1975; Lamers & Cassinelli, 1999). The efficiency of this momentum transfer is given by (Lamers & Cassinelli, 1999):

$$\eta_{\mathrm{mom}} = \frac{\dot{M} v_\infty}{L/c}, \tag{3.3}$$

where $\dot{M}$ is the stellar mass loss rate, v_∞ is the wind's terminal velocity, and L is the stellar luminosity. Since the momentum of the wind originates from radiation, momentum conservation dictates that the total pressure after transfer equates to the radiation pressure from the star, i.e., $P_{\mathrm{tot}} = P_{\mathrm{sw}} + P_{\mathrm{rad}} = \frac{L}{4\pi r^2 c}$. Consequently, the

ratio of stellar wind ram pressure $P_{sw} = \frac{\dot{M}v_\infty}{4\pi r^2}$ to radiation pressure $P_{rad} = \frac{L}{4\pi r^2 c} - \frac{\dot{M}v_\infty}{4\pi r^2}$ is expressed as:

$$\frac{P_{sw}}{P_{rad}} = \frac{\eta_{mom}}{1 - \eta_{mom}}. \tag{3.4}$$

Lamers & Cassinelli (1999) investigated the winds of five typical early-type stars and found that, except for Wolf–Rayet stars, η_{mom} values for Xi Pup, Epsilon Orionis, P Cygni, and Tau Scorpii are approximately 0.2, indicating that ram pressure and radiation pressure are comparable for these stars. The total force exerted on a particle of size a is given by:

$$F_{tot} = P_{sw} \langle Q_{sw} \rangle \pi a^2 + P_{rad} \langle Q_{pr} \rangle \pi a^2$$

$$= P_{tot} \alpha_{rad} \pi a^2, \tag{3.5}$$

where

$$\alpha_{rad} = \frac{P_{sw} \langle Q_{sw} \rangle + P_{rad} \langle Q_{pr} \rangle}{P_{sw} + P_{rad}}$$

$$= \eta_{mom} \langle Q_{sw} \rangle + (1 - \eta_{mom}) \langle Q_{pr} \rangle. \tag{3.6}$$

Thus, the ratio of the total force to gravitational force is given by (Burns et al., 1979; Hoang et al., 2021):

$$\beta = \frac{3L\alpha_{rad}}{16\pi G M c a \rho}$$

$$= 0.19 \frac{L}{L_\odot} \frac{M_\odot}{M} \frac{\alpha_{rad}}{1} \frac{3\,\text{g/cm}^3}{\rho} \frac{1\,\mu\text{m}}{a}, \tag{3.7}$$

where $L/L_\odot$ and $M/M_\odot$ are the stellar luminosity and mass in solar units.

The total photogravitational force is given by (Krivov et al., 2006):

$$F_{pg} = -\frac{GM(1-\beta)m}{r^3}\mathbf{r},\qquad(3.8)$$

where G is the gravitational constant, M is the stellar mass, and m is the particle mass. A particle becomes unbound when $\beta > 1$, and fragments released from a circular orbit become unbound if $\beta > 0.5$ (Krivov et al., 2006). Combining Equations 2.35 and 3.8, and assuming a particle is released at rest, the derivative of its rotational velocity ω with respect to distance r is:

$$\frac{d\omega}{dr} = \frac{1}{\sqrt{2GM(\beta-1)}}\sqrt{\frac{r_0 r}{(r-r_0)}}\frac{\Gamma_{\mathrm{RAT}}}{I}\left(1 - \frac{\omega}{\omega_{\mathrm{RAT}}}\right).\qquad(3.9)$$

Empirical data suggest that the mass-luminosity relation follows $\beta \propto L \propto M^\zeta$, $\Gamma_{\mathrm{RAT}} \propto L \propto M^\zeta$, and $\omega_{\mathrm{RAT}} \propto L^{1/3} \propto M^{\zeta/3}$. Assuming $\beta \gg 1$, Equation 3.9 suggests that higher-mass stars induce faster particle disruption if $\zeta > 1$. Observational studies indicate that for stars with solar composition, ζ varies between 2.6 and 4.5 for masses between ~0.2 and $20\,\mathrm{M_\odot}$ (Salaris & Cassisi, 2005).

Since radiation pressure depends on particle properties, Wilck & Mann (1996) computed β-values for different dust models, showing that only young cometary particles have $\beta > 1$. Other studies (e.g., Arnold et al., 2019; Sterken et al., 2019) corroborate this by demonstrating that water ice and porous silicate grains in the Solar System have $\beta < 1$, whereas mixed ice, carbon, and silicate compositions can exceed $\beta = 1$. However, our results suggest that RATD effectively disrupts particles larger than $0.1\,\mu\mathrm{m}$ before they can be expelled by radiation pressure.

For β-meteoroids, assuming release from a parent body at heliocentric distance

Figure 3.10: Critical rotational velocities (ω, dashed lines) and the maximum rotational velocities (ω_{disr}, solid lines) that the β-meteoroids can reach during the journey between $1\,\text{au}$ and $100\,\text{au}$ when released on a circular orbit at $1\,\text{au}$ with different particle sizes (a), tensile strengths (S_{eff}) and β-values.

r_0 on circular orbits (Wehry & Mann, 1999), the radial velocity is:

$$v_r = \sqrt{-\frac{2GM(\beta-1)}{r} - \frac{l^2}{r^2} + \frac{GM}{r_0} + \frac{2GM(\beta-1)}{r_0}}, \qquad (3.10)$$

where $l = \sqrt{GMr_0}$ is the meteoroid's specific angular momentum. The derivative of rotational velocity is then:

$$\frac{d\omega}{dr} = \frac{1}{v_r}\frac{\Gamma_{\text{RAT}}}{I}\left(1 - \frac{\omega}{\omega_{\text{RAT}}}\right). \qquad (3.11)$$

Fig. 3.10 shows the critical rotational velocities ω_{disr} (dashed line) and the maximum rotational velocities ω_{max} (solid line) that β-meteoroids can reach during the journey between $1\,\text{au}$ and $100\,\text{au}$ when they are released at $1\,\text{au}$ with different particle sizes and β-values. The result indicates that β-meteoroids trapped in a high-J attractor point with sizes between $0.1\,\mu\text{m}$ to $1\,\mu\text{m}$ will be disrupted before reaching $100\,\text{au}$.

55

3.7 Location of Disruption in the Presence of Radiation Pressure

The heliocentric distance at which a particle is disrupted due to radiative torques, denoted as r_d, depends on its initial release distance r_0. The displacement interval between the initial location and the disruption location is given by $\Delta r = r_d - r_0$, leading to:

$$r_d = r_0 + \Delta r. \tag{3.12}$$

To estimate r_d, we assume that $\Delta r \ll r_0$, allowing us to approximate the acceleration and disruption timescales as locally constant. Under this assumption, the displacement interval can be expressed as:

$$\Delta r \approx v_{r0} t_{\text{disr}} + \frac{1}{2}\left[\frac{(\beta-1)GM}{r^2} + \frac{l^2}{r^3}\right]_{r=r_0} t_{\text{disr}}^2(r_0), \tag{3.13}$$

where v_{r0} is the radial velocity of the particle at release, and $a_r = \frac{(\beta-1)GM}{r^2} + \frac{l^2}{r^3}$ is the radial acceleration.

For a particle released at rest ($v_{r0} = 0$ and $l = 0$), using the gravitational constant $G = \frac{4\pi^2}{M_\odot}\frac{1\,\text{au}^3}{1\,\text{yr}^2}$, the disruption location simplifies to:

$$r_d \approx r_0 + 2\pi^2(\beta-1)\left(\frac{M}{M_\odot}\right)\left(\frac{1\,\text{au}}{r_0}\right)^2\left(\frac{t_{\text{disr}}}{1\,\text{yr}}\right)^2 \text{ au}. \tag{3.14}$$

For a particle released from a circular orbit ($v_{r0} = 0$ and $l = \sqrt{GMr_0}$), the disruption

56

location is:

$$r_d \approx r_0 + 2\pi^2 \beta \left(\frac{M}{M_\odot}\right)\left(\frac{1\,\text{au}}{r_0}\right)^2 \left(\frac{t_\text{disr}}{1\,\text{yr}}\right)^2 \text{ au.} \qquad (3.15)$$

Thus, the condition $\Delta r \ll r_0$ requires:

$$\left(\frac{M}{M_\odot}\right)\left(\frac{1\,\text{au}}{r_0}\right)^3 \left(\frac{t_\text{disr}}{1\,\text{yr}}\right)^2 \ll 1. \qquad (3.16)$$

From the above, we find that $\Delta r \propto t_\text{disr}^2/r_0^2$. If the condition $\omega_\text{RAT} \gg \omega_\text{disr}$ holds, then, using Equations 2.38 and 2.39 for a fixed β, the displacement interval follows:

$$\Delta r \propto \begin{cases} r_0^2 S a^{-1.4}, & a \lesssim \bar{\lambda}/1.8 \\[2mm] r_0^2 S a^4, & a > \bar{\lambda}/1.8 \end{cases}. \qquad (3.17)$$

This implies that the ratio $\Delta r/r_0$ decreases with decreasing r_0, making the condition $\Delta r \ll r_0$ easier to satisfy.

The location of disruption can also be determined numerically using Equations 3.11 and 2.28. Figures 3.12 and 3.13 show the heliocentric distance at which a particle is disrupted by RATD, corresponding to the cases presented in Figures 3.11 and 3.10, respectively. As predicted by Equation 3.17, the displacement interval Δr increases more rapidly for a particle with size a increasing from $\bar{\lambda}/1.8$ than for decreasing a. Additionally, Δr increases with effective tensile strength S_eff.

Figures 3.12 and 3.13 further illustrate that for particles in the $\omega > \omega_\text{disr}$ regime, the disruption location is close to the release distance. The steep slope observed at the boundary of this regime suggests that RATD effectively disrupts particles before
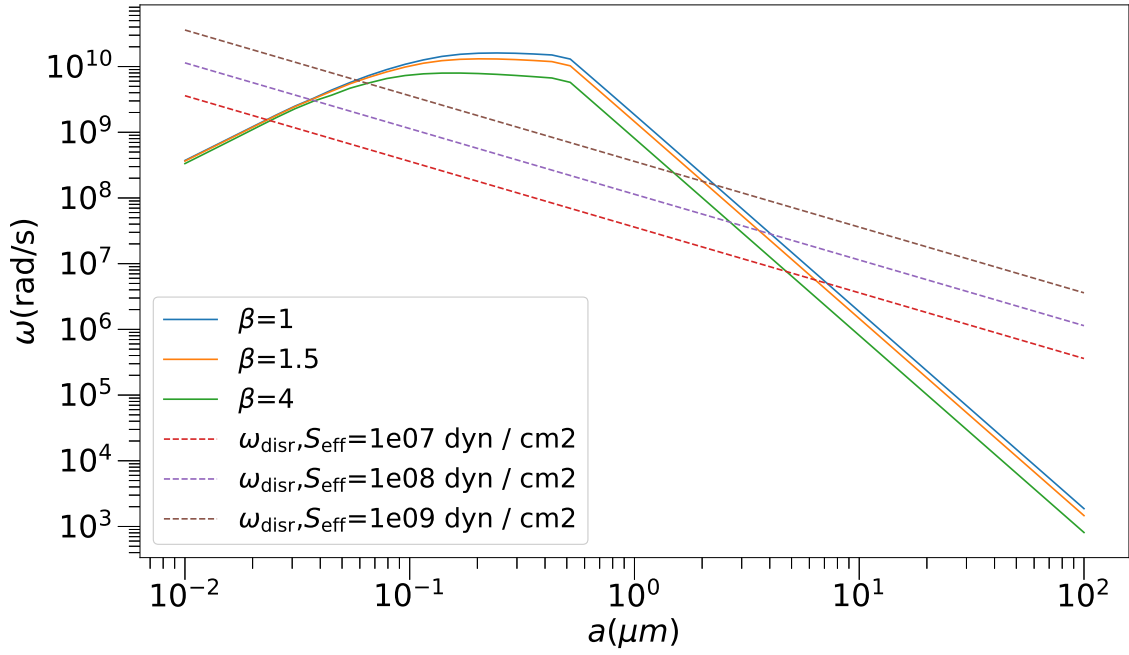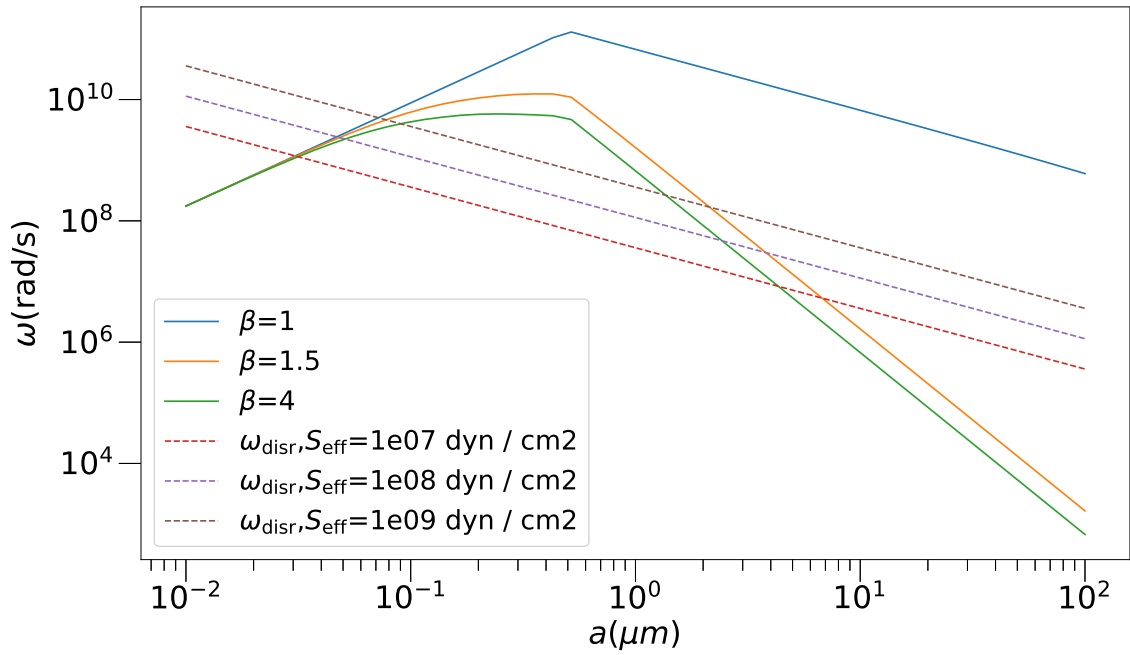
Figure 3.11: Critical rotational velocities (ω, dashed lines) and the maximum rotational velocities (ω_{disr}, solid lines) of the particles released at rest at $1\,\mathrm{au}$ and before reaching $r = 100\,\mathrm{au}$ with different particle sizes (a), tensile strengths (S_{eff}) and β-values. β is defined in Equation 3.7.

they are expelled by radiation pressure.
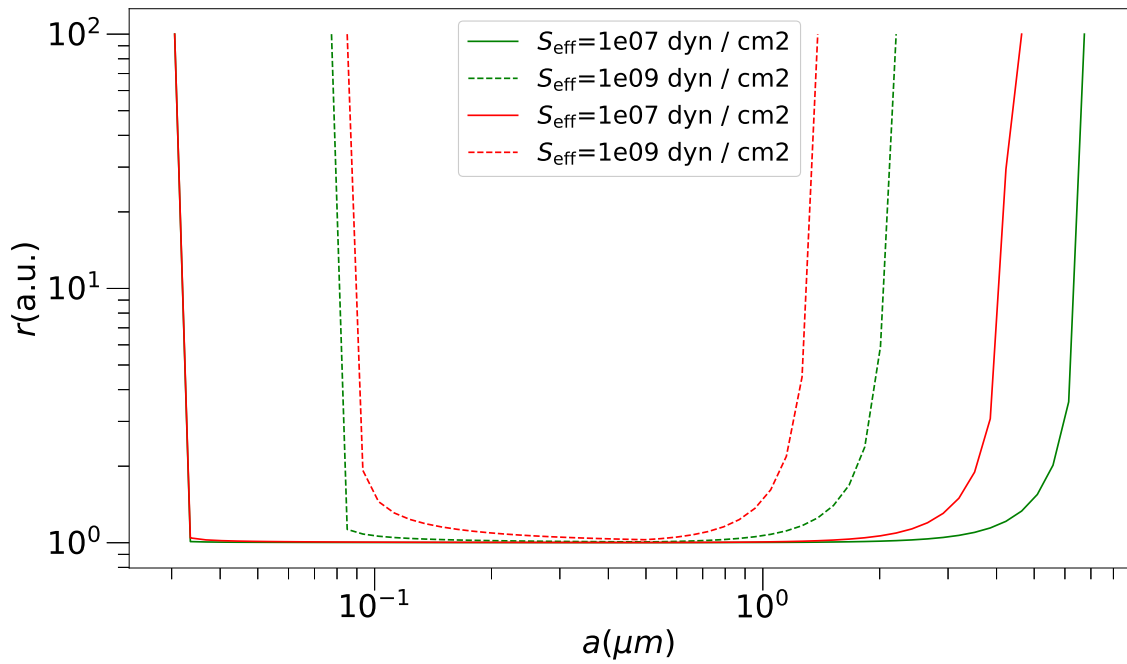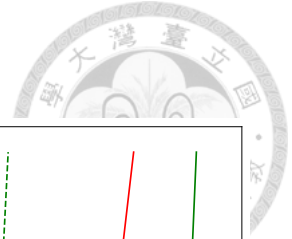
Figure 3.12: Disruption location (r) of a particle released at rest at $1\,\mathrm{au}$, for different particle sizes (a), β-values, and tensile strengths (S_{eff}).
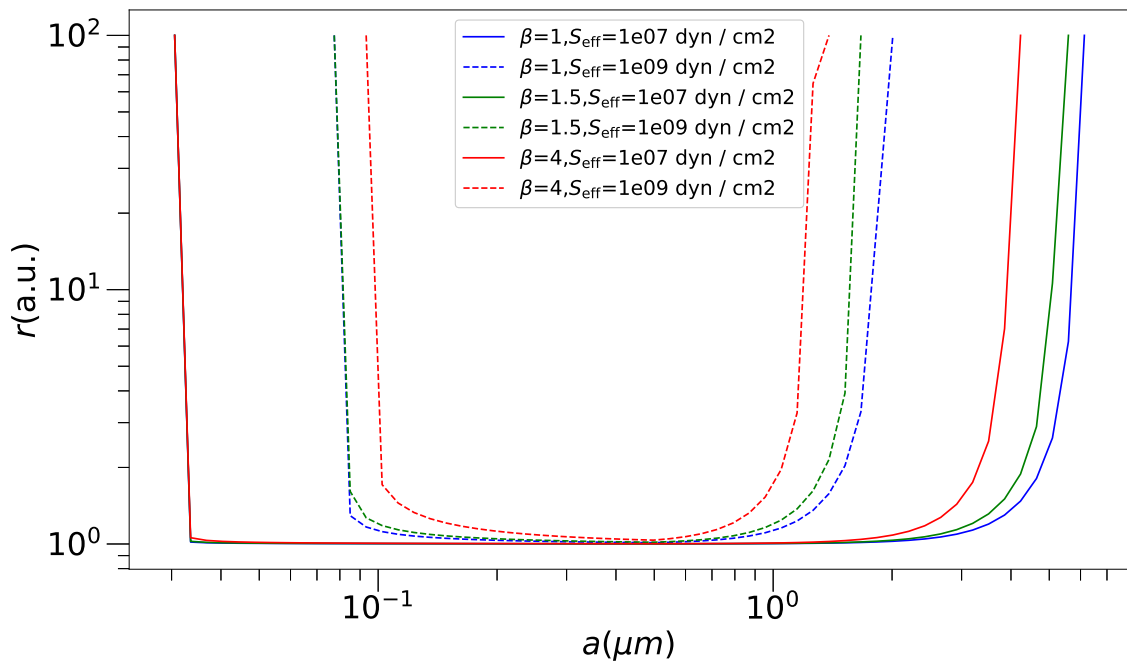
Figure 3.13: Disruption location (r) of a particle released in a circular orbit at $1\,\mathrm{au}$, for different particle sizes (a), β-values, and tensile strengths (S_{eff}).
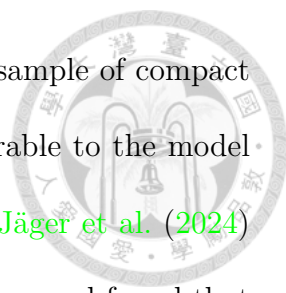
Chapter 4 Discussion

In this section, we outline the approaches for assessing the RATD theory's impact on dust dynamics within the heliosphere. We also discuss the necessity of in-situ measurements to determine grain size and composition and validate the RATD theory by analyzing dust properties at varying distances from the Sun. Ground-based experiments on samples from missions such as Hayabusa and Stardust are proposed to estimate dust tensile strength and angular velocities, enhancing our understanding of nanoparticle formation. The evolution of debris disks is examined, with a focus on how RATD may explain high infrared luminosities observed in systems like HD 113766 by producing nanoparticles at elevated rates. Additionally, we discuss the uncertainties and limitations of our simple models for investigating the evolution of dust size and spatial distributions.

4.1 Comparison of RAT Efficiency Models and Their Impact on Grain Disruption

In this study, we use the parametric function of the RAT efficiency from Lazarian & Hoang (2007), i.e., Equation 2.17, which was derived by fitting numerical calculations of RATs using DDSCAT (Draine & Flatau, 2008) for several grain shapes.

61

Herranen et al. (2019) calculated the RAT efficiency for a large sample of compact grain shapes and found that the mean RAT efficiency is comparable to the model of Lazarian & Hoang (2007) (see their Fig. 20). More recently, Jäger et al. (2024) extended these calculations to include more porous grain structures and found that the RAT efficiency for such shapes is lower than predicted by the Lazarian & Hoang (2007) model. However, they also concluded that rotational disruption can still occur when the local radiation field is more than 100 times stronger than the typical interstellar radiation field. Given the much stronger solar radiation field, our results for grain disruption based on the Lazarian & Hoang (2007) model remain largely unaffected even if the RAT efficiency for dust aggregates from Jäger et al. (2024) is adopted.

4.2   In-Situ Dust Measurements and Future Missions

To verify the location of the present water snow line for different grain sizes, in-situ measurement of the size and composition of the grains is required. Although the distribution of grain size in the Solar System inside 5 au has been obtained from multiple measurements (Equation 2.11), how the composition of nanodust changes with radius remains unclear. The highly sensitive dust instrumentation developed in concept missions, such as DuneXpress in the past (Grün et al., 2009), would allow us to measure the mass and elemental composition simultaneously. Therefore, we can obtain the number density with different tensile strengths and sizes at 1 au. Moreover, precise size-dependent dust flux measurements provided by DuneXpress would enable us to acquire accurate data to verify the RATD theory at 1 au (Grün et al., 2009).
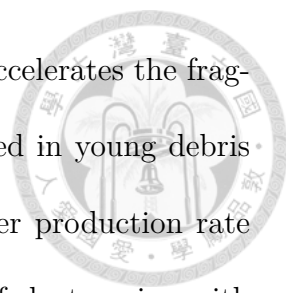
Another concept mission, the Interstellar Probe, will also be equipped with dust composition analyzers capable of measuring the impactor fluxes for interplanetary and interstellar grains and measuring the composition of IPD and ISD grains (Interstellar Probe Study Team, 2021). Since the space probe is expected to leave the Solar System, it can measure the mass, speed, and composition of the impacting dust particles at the location of the present water snow line.

4.3   Ground-Based Measurements

Laboratory experiments can be conducted on samples collected by in-situ instruments on spacecraft such as Hayabusa and Stardust. For example, the tensile strength of the ISD can be estimated by measuring the critical angular velocity. Abbas et al. (2004) measured the angular velocity of SiC particles by analyzing the low-frequency signal of the scattered light. Additionally, a high angular velocity could be measured by Rotational X-ray Tracking (RXT) (Liang et al., 2018). Since RXT has a resolution of tens of microradians, with microsecond time resolution, it can potentially resolve the dust grains with an angular velocity of $10^9 \, \mathrm{rad \, s^{-1}}$, which is the critical rotational velocity for micrometer-sized dust (Equation 2.28). Confirmation or refutation of this would greatly improve our understanding of nanoparticle formation in the Solar System.

4.4   Dust Evolution in Debris Disks
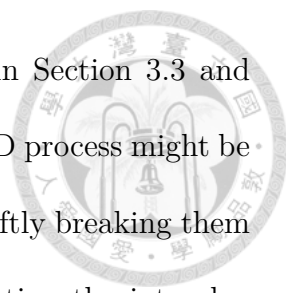
A debris disk is formed at the end of the protoplanetary disk phase, during which the gas-to-dust mass ratio becomes low. It is usually optically thin, so a

63

strong radiation field is considered. Since rotational disruption accelerates the fragmentation process, we expect that nanoparticles can be produced in young debris disks and in the debris disks around early-type stars at a higher production rate than in the Solar System. Additionally, the number density of dust grains with sizes between $0.1\,\mu\mathrm{m}$ and $100\,\mu\mathrm{m}$ would be much lower than the number density produced by grain-grain collisions alone. In contrast, the number density of sub-μm-sized dust grains will be higher than the number density produced by grain-grain collisions alone.

This might help solve the problem of systems like HD 113766, where the observed infrared fractional luminosity of the inner belt is much higher than the maximum value for a steady state in typical collisional cascades (Su et al., 2020). The outer belt of the system is not affected by RATD because the disk is optically thick to solar wind in the early stage of the planetesimal disk (Wetherill, 1981). Consequently, sub-μm-sized dust grains created in the inner belt are unable to be transported to the outer belt effectively. Additionally, the NIR excess from early-type stars has been modeled as thermal emissions from hot nanoparticles in the vicinity of the stars (Su et al., 2013).

Moreover, the silicate solid-state features at the wavelength of $10\,\mu\mathrm{m}$ from some young early-type stars can be attributed to sub-micron particles (Su et al., 2013, 2020). Later, Rieke et al. (2016) showed that nanoparticles can be trapped by a dipole magnetic field. On the other hand, Stamm et al. (2019) showed that sub-micron-sized particles are expected to be removed in a short time due to the fast radiation blowout of early-type stars with a Parker spiral model. Consequently, Mann (2017) suggested that comets might contribute to nanoparticle production.

Although it might not solve the entire puzzle, our study in Section 3.3 and discussion in 3.7 provide a mechanism where the even faster RATD process might be able to avoid the removal barriers of micron-sized particles by swiftly breaking them down to nanoparticles, thus increasing their number. Investigating the interplay between collisional cascade, PR drag, stellar winds, RATD, gas components (e.g., Lebreton et al., 2013), and impact events (e.g., Su et al., 2020) for nanoparticle production and loss remains a compelling direction for future studies.

4.5 Limitations of Our Theoretical Investigation

For larger particles ($> 10^2 \, \mu$m), the numerical results in Fig. 3.3 indicate that the slope of the size distribution at $1 \, \text{au}$ differs from the in-situ measurement from Grün et al. (1985). The discrepancy could be attributed to the limited sources of larger particles (i.e., which is modelled using one free parameter $\dot{m}_{\text{b}}^-$ in our simple analysis) and the influence of the Earth's gravitational field that sweeps IDPs (e.g., Jorgensen et al., 2021).

Conversely, while models based on infrared emission from the zodiacal dust cloud provide the spatial distribution of micrometer-sized dust (Rowan-Robinson & May, 2013), sub-μm-sized dust grains are unlikely to follow the same distribution. These smaller grains, with their high charge-to-mass ratios, are significantly affected by magnetic forces. Therefore, they can be captured and carried away by solar winds (e.g., Czechowski & Mann, 2010; Juhász & Horányi, 2013; O'Brien et al., 2014, 2018). Consequently, as noted in Section 2, for these charged nanodust, their high-speed trajectories are preferentially detected by plasma wave instruments and

are not modeled in the present study. Moreover, because the Sun's magnetic field fluctuates over time, these particles are expected to be displaced from the zodiacal plane (e.g., Chiang & Fung, 2017; Mukai & Giese, 1984). As a result, the number density of dust grains decreases, leading to a lower mass loss rate from grain-grain collisions. Besides magnetic effects, solar winds may destruct small grains through nonthermal sputtering (Hoang et al., 2021).

For β-meteoroids that trapped in a low-J attractor, they will not be disrupted by RATD and PR drag, and will only be disrupted by collisions with other grains. However, given the large timescale for collision disruption shown in Fig. 3.1, these β-meteoroids will likely be pushed outward from the heliosphere into interstellar space before they experience collisions.

While more sophisticated modeling is reserved for future studies, it is important to highlight that, although the loss rate of sub-μm-sized dust grains remains uncertain, their production rate can be calculated as detailed in Section 2.10, where RATD is considered in a dust collisonal cascade model for the first time. This information is essential for guiding future research.
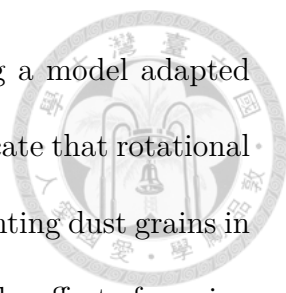
Chapter 5 Summary

The majority of the content in this thesis is based on Ng et al. (2025). This work explores the lifetime of dust grains in the heliosphere by applying the RATD mechanism and have incorporated this mechanism into the dust size distribution model proposed by Wyatt et al. (2011). We have also studied the effect of RATD on the dust strongly subject to radiation pressure. Our main results are summarized as follows:

1. We have calculated the characteristic disruption timescales due to radiative torque for various tensile strengths of dust. Our results show that large particles (ranging from $>0.1\,\mu$m to $<10^3\,\mu$m)) can indeed be fragmented into nanoparticles (less than $50\,$nm) within the heliosphere (less than $100\,$au), regardless of their distance from the Sun.

2. The LISM affects the rotational disruption size and time in the outer heliosphere (i.e., $> 10\,$au). Specifically, it significantly impacts the maximum disruption size while slightly influencing the minimum disruption size. Therefore, we conjecture that micrometer-sized dust can be fractured into nanoparticles by RATD within the entire heliosphere. RATD plays an important role in shaping the size distribution of μm-sized dust.

3. We computed the steady-state dust size distribution using a model adapted from the framework of Wyatt et al. (2011). Our results indicate that rotational disruption is the primary mechanism responsible for fragmenting dust grains in the size range of $0.1\,\mu\mathrm{m}$ to $10^3\,\mu\mathrm{m}$. We further investigated the effect of varying the fraction of grains aligned at high-J attractor points. The comparison shows that for $f_{\mathrm{highJ}} = 1$, the mass distribution of large grains is substantially reduced, while the abundance of nanodust grains increases by several orders of magnitude. In cases where $1 > f_{\mathrm{highJ}} > 0.5 - 0.8$, the modification to the mass distribution is weaker but still significant.

4. We have calculated the present locations of the water snow line for different grain sizes and found that the snow line of large dust grains can exceed the limit imposed by the sublimation temperature of water ice.

5. We have shown that for a dust grain with a constant β-value, increasing the star's luminosity will not cause the particle to be expelled if the dust remains trapped in a high-J attractor. In this case, the particle is disrupted more rapidly by radiative torque compared to being blown out by radiation pressure. Therefore, detected β-meteoroids should be trapped in a low-J attractor in our model.

68

References

Abbas M. M., et al., 2004, The Astrophysical Journal, 614, 781

Ahles A. A., Emery J. D., Dunand D. C., 2021, Acta Astronautica, 189, 465

Arnold J. A., Weinberger A. J., Videen G., Zubko E. S., 2019, The Astronomical Journal, 157, 157

Baranov V. B., Malama Y. G., 1995, Journal of Geophysical Research, 100, 14755

Bhowmik T., et al., 2019, Astronomy & Astrophysics, 630, A85

Bockelee-Morvan D., 2015, Proceedings of the International Astronomical Union, 11, 401

Burns J. A., Lamy P. L., Soter S., 1979, Icarus, 40, 1

Castor J. I., Abbott D. C., Klein R. I., 1975, The Astrophysical Journal, 195, 157

Chiang E., Fung J., 2017, The Astrophysical Journal, 848, 4

Ciardi D. R., van Belle G. T., Akeson R. L., Thompson R. R., Lada E. A., Howell S. B., 2001, The Astrophysical Journal, 559, 1147

Czechowski A., Mann I., 2010, The Astrophysical Journal, 714, 89

DeMeo F. E., Carry B., 2014, Nature, 505, 629

Defrère D., et al., 2011, Astronomy & Astrophysics, 534, A5

Divine N., 1993, Journal of Geophysical Research, 98, 17029

Djurišić A. B., Li E. H., 1999, Journal of Applied Physics, 85, 7404

Dolginov A. Z., Mitrofanov I. G., 1976, Ap&SS, 43, 291

Draine B. T., Flatau P. J., 2008, Journal of the Optical Society of America A, 25, 2693

Draine B. T., Lazarian A., 1998, The Astrophysical Journal, 508, 157

Draine B. T., Weingartner J. C., 1997, The Astrophysical Journal, 480, 633

Egger R. J., Freyberg M. J., Morfill G. E., 1996, Space Science Reviews, 75, 511

Friedlander S. K., 2000, Smoke, Dust, and Haze: Fundamentals of Aerosol Dynamics, 2nd edition edn. Oxford University Press, New York

Geiss J., Gloeckler G., von Steiger R., 1996, Space Science Reviews, 78, 43

Gopalswamy N., Hasan S., Ambastha A., eds, 2010, Heliophysical Processes. Astrophysics and Space Science Proceedings, Springer Berlin Heidelberg, Berlin, Heidelberg, doi:10.1007/978-3-642-11341-3, http://link.springer.com/10.1007/978-3-642-11341-3

Grün E., Zook H. A., Fechtig H., Giese R. H., 1985, Icarus, 62, 244

Grün E., et al., 2009, Experimental astronomy, 23, 981

Gundlach B., et al., 2018, Monthly Notices of the Royal Astronomical Society, 479, 1273

Haack D., Otto K., Gundlach B., Kreuzig C., Bischoff D., Kührt E., Blum J., 2020, Astronomy & Astrophysics, 642, A218
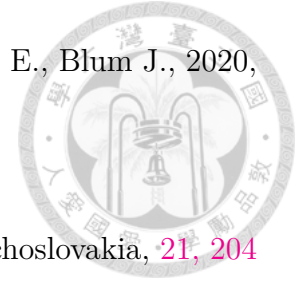
Harwit M., 1970, Bulletin of the Astronomical Institutes of Czechoslovakia, 21, 204

Henin B., 2018, Exploring the Ocean Worlds of Our Solar System. Springer Cham, Switzerland, doi:10.1007/978-3-319-93476-1, https://www.springer.com/gp/book/9783319934754

Herranen J., Lazarian A., Hoang T., 2019, The Astrophysical Journal, 878, 96

Herranen J., Lazarian A., Hoang T., 2021, The Astrophysical Journal, 913, 63

Hoang T., 2019, The Astrophysical Journal, 876, 13

Hoang T., Lazarian A., 2008, Monthly Notices of the Royal Astronomical Society, 388, 117

Hoang T., Lazarian A., 2014, Monthly Notices of the Royal Astronomical Society, 438, 680

Hoang T., Lazarian A., 2016, The Astrophysical Journal, 831, 159

Hoang T., Lee H., 2019, The Astrophysical Journal, 896, 144

Hoang T., Loeb A., 2017, The Astrophysical Journal, 848, 31

Hoang T., Tram L. N., 2020, The Astrophysical Journal, 891, 38

Hoang T., Vinh N.-A., Lan N. Q., 2016, The Astrophysical Journal, 824, 18

Hoang T., Tram L. N., Lee H., Ahn S.-H., 2019, Nature Astronomy, 3, 766

Hoang T., Lazarian A., Lee H., Cho K., Gu P.-G., Ng C.-H., 2021, The Astrophysical Journal, 919, 91

Hoang T., Minh Phan V. H., Tram L. N., 2023, The Astrophysical Journal, 954, 216

Horányi M., 1996, Annual Review of Astronomy and Astrophysics, 34, 383

Howatson A. M., Lund P. G., Todd J. D., 1972, Engineering Tables and Data. Springer Netherlands, Dordrecht, doi:10.1007/978-94-010-9314-9, http://link.springer.com/10.1007/978-94-010-9314-9

Hsieh H. H., Jewitt D., 2006, Science, 312, 561

Hsu H.-W., et al., 2018, Science, 362, eaat3185

Interstellar Probe Study Team 2021, Interstellar Probe Study 2019 Report. Johns Hopkins University Applied Physics Laboratory, Maryland, USA, https://interstellarprobe.jhuapl.edu/uploadedDocs/papers/588-ISP-Study-2019-Report_PR.pdf

Ipatov S. I., Kutyrev A. S., Madsen G. J., Mather J. C., Moseley S. H., Reynolds R. J., 2008, Icarus, 194, 769

Izmodenov V. V., Kallenbach R., 2006, The physics of the heliospheric boundaries. ESA Publications Division, The Netherlands

Jorgensen J. L., Benn M., Connerney J. E. P., Denver T., Jorgensen P. S., Andersen A. C., Bolton S. J., 2021, Journal of Geophysical Research: Planets, 126, e06509

Juhász A., Horányi M., 2013, Geophysical Research Letters, 40, 2500

Jäger J. A., Reissl S., Klessen R. S., 2024, Astronomy & Astrophysics, 692, A244

Kadish J., Barber J. R., Washabaugh P. D., 2005, International Journal of Solids and Structures, 42, 5322

Keller L. P., Flynn G. J., 2022, Nature Astronomy, 6, 731

Kempf S., 2008, Planetary and Space Science, 56, 378

Kimura H., Mann I., 1998, The Astrophysical Journal, 499, 454

Kimura H., et al., 2020, Monthly Notices of the Royal Astronomical Society, 496, 1667

Kitamura R., Pilon L., Jonasz M., 2007, Applied Optics, 46, 8118

Krivov A., Löhne T., Sremčević M., 2006, Astronomy & Astrophysics, 455, 509

LLera K., Burch J., Goldstein R., Goetz C., 2020, Geophysical Research Letters, 47, e2019GL086147

Lamers H. J. G. L. M., Cassinelli J. P., 1999, Introduction to Stellar Winds, 1 edn. Cambridge University Press, doi:10.1017/CBO9781139175012, https://www.cambridge.org/core/product/identifier/9781139175012/type/book

Lazarian A., 2020, The Astrophysical Journal, 902, 97

Lazarian A., Draine B. T., 1999, The Astrophysical Journal, 520, L67

Lazarian A., Hoang T., 2007, Monthly Notices of the Royal Astronomical Society, 378, 910

Lebreton J., et al., 2013, Astronomy & Astrophysics, 555, A146

Leinert C., Richter I., Pitz E., Planck B., 1981, Astronomy and Astrophysics, 103, 177

Lhotka C., Narita Y., 2019, Annales Geophysicae, 37, 299

Liang M., Harder R., Robinson I., 2018, Journal of Synchrotron Radiation, 25, 757

Love S., Brownlee D., 1993, Science, pp 550–553

Mann I., 2017, Philosophical Transactions of the Royal Society A: Mathematical, Physical and Engineering Sciences, 375

Mann I., et al., 2004, Space Science Reviews, 110, 269

Mann I., Murad E., Czechowski A., 2007, Planetary and Space Science, 55, 1000

Mann G., Warmuth A., Vocks C., Rouillard A. P., 2023, Astronomy & Astrophysics, 679, A64

Mannel T., et al., 2019, Astronomy & Astrophysics, 630, A26

Mathis J., Mezger P., Panagia N., 1983, Astronomy and Astrophysics, 128, 212

McComas D. J., et al., 2015, The Astrophysical Journal, 801, 28

Meyer-Vernet N., et al., 2009, Solar Physics, 256, 463

Min M., Dullemond C., Kama M., Dominik C., 2011, Icarus, 212, 416

Minato T., Köhler M., Kimura H., Mann I., Yamamoto T., 2004, Astronomy & Astrophysics, 424, L13

Minato T., Köhler M., Kimura H., Mann I., Yamamoto T., 2006, Astronomy & Astrophysics, 452, 701

Morbidelli A., Chambers J., Lunine J. I., Petit J. M., Robert F., Valsecchi G. B., Cyr K. E., 2000, Meteoritics & Planetary Science, 35, 1309

Mukai T., Giese R. H., 1984, Astronomy and Astrophysics, 131, 355

Musiolik G., Beule C. d., Wurm G., 2017, Icarus, 296, 110

Nesvornỳ D., Jenniskens P., Levison H. F., Bottke W. F., Vokrouhlickỳ D., Gounelle M., 2010, The Astrophysical Journal, 713, 816

Ng C.-H., Gu P.-G., Hoang T., 2025, Monthly Notices of the Royal Astronomical Society, 538, 1944

O'Brien L., et al., 2014, Review of Scientific Instruments, 85, 035113

O'Brien L., Juhász A., Sternovsky Z., Horányi M., 2018, Planetary and Space Science, 156, 7

O'Shea E., Sternovsky Z., Malaspina D. M., 2017, Journal of Geophysical Research: Space Physics, 122, 11864

Owens M. J., Forsyth R. J., 2013, Living Reviews in Solar Physics, 10, 5

Pedersen B. M., Meyer-Vernet N., Aubier M. G., Zarka P., 1991, Journal of Geophysical Research, 96, 19187

Petrovic J. J., 2003, Journal of Materials Science, 38, 1

Podolak M., Zucker S., 2004, Meteoritics and Planetary Science, 39, 1859

Postberg F., Kempf S., Srama R., Green S., Hillier J., Mcbride N., Grun E., 2006, Icarus, 183, 122

Prockter L. M., 2005, Johns Hopkins APL Technical Digest (Applied Physics Laboratory), 26, 175

Purcell E. M., 1979, The Astrophysical Journal, 231, 404

Rieke G. H., Gaspar A., Ballering N. P., 2016, The Astrophysical Journal, 816, 50

Rowan-Robinson M., May B., 2013, Monthly Notices of the Royal Astronomical Society, 429, 2894

Salaris M., Cassisi S., 2005, Evolution of stars and stellar populations. J. Wiley, Chichester, West Sussex, England ; Hoboken, NJ, USA

Schippers P., et al., 2015, The Astrophysical Journal, 806, 77

Seki J., Hasegawa H., 1983, Astrophysics and Space Science, 94, 177

Slavin J. D., Frisch P. C., Müller H.-R., Heerikhuisen J., Pogorelov N. V., Reach W. T., Zank G., 2012, The Astrophysical Journal, 760, 46

Stamm J., Czechowski A., Mann I., Baumann C., Myrvang M., 2019, Astronomy & Astrophysics, 626, A107

Sterken V. J., Westphal A. J., Altobelli N., Malaspina D., Postberg F., 2019, Space Science Reviews, 215, 43

Su K. Y. L., et al., 2013, The Astrophysical Journal, 763, 118

Su K. Y. L., Rieke G. H., Melis C., Jackson A. P., Smith P. S., Meng H. Y. A., Gáspár A., 2020, The Astrophysical Journal, 898, 21

Tatsuuma M., Kataoka A., Tanaka H., 2019, The Astrophysical Journal, 874, 159

Tram L. N., Hoang T., 2022, Frontiers in Astronomy and Space Sciences, 9, 923927

Tsuchiyama A., Mashio E., Imai Y., Noguchi T., Miura Y., Yano H., Nakamura T., 2009, Meteoritics and Planetary Science Supplement, 72, 5189

Voshchinnikov N., 1990, Soviet Astronomy, 34, 429

Warren S. G., Brandt R. E., 2008, Journal of Geophysical Research, 113, D14220

Wehry A., Mann I., 1999, Astronomy and Astrophysics, 341, 296

Weingartner J. C., 2006, The Astrophysical Journal, 647, 390

Wetherill G. W., 1981, Icarus, 46, 70

Wilck M., Mann I., 1996, Planetary and Space Science, 44, 493

Wyatt M. C., Clarke C. J., Booth M., 2011, Celestial Mechanics and Dynamical Astronomy, 111, 1

Ye S., Gurnett D., Kurth W., 2016, Icarus, 279, 51

Zhang Y., Zhang Y., Guo R., Cui B., 2022, Water, 14, 1363

Ziegler J. F., Ziegler M., Biersack J., 2010, Nuclear Instruments and Methods in Physics Research Section B: Beam Interactions with Materials and Atoms, 268, 1818

Zubko E., 2013, Earth, Planets and Space, 65, 139

van Lieshout R., Dominik C., Kama M., Min M., 2014, Astronomy & Astrophysics, 571, A51

Appendix A — Characteristic Damping Time

Assume that the gas reaches thermal equilibrium, so the gas thermal velocity follows the Boltzmann distribution with a constant drift velocity v_{d}, given by:

$$f(\boldsymbol{v}) = \left(\frac{m}{2\pi kT}\right)^{3/2} e^{-m(\boldsymbol{v}-\boldsymbol{v}_d)^2/2kT}. \tag{A.1}$$

We also assume the dust particles are spherical, with the surface defined by spherical coordinates (a, θ', ϕ'), where a is the radius of the sphere. Without loss of generality, assume the direction of the drift velocity along $\theta' = 0$.

The number of particles passing through the area dA with the speeds in the interval $[v, v + dv]$ over the time dt is given by:

$$\frac{dN}{dt} = n \int_0^\pi \int_0^\infty \int_0^{2\pi} \int_0^{\frac{\pi}{2}} v \cos\theta f(\boldsymbol{v}) d\theta d\phi v^2 \sin\theta dv \times$$
$$2\pi a^2 \sin\theta' d\theta', \tag{A.2}$$

$$\frac{dN}{dt} = n \int_0^\pi \int_0^\infty \int_0^{2\pi} \int_0^{\frac{\pi}{2}} v^3 \sin\theta \cos\theta \left(\frac{1}{v_{\mathrm{th}}^2 \pi}\right)^{3/2} \times$$
$$e^{-(v^2 - 2vv_{\mathrm{d}} \sin\theta \sin\theta' \cos\phi - 2vv_{\mathrm{d}} \cos\theta \cos\theta' + v_{\mathrm{d}}^2)/v_{\mathrm{th}}^2} \times \tag{A.3}$$
$$d\theta d\phi dv 2\pi a^2 \sin\theta' d\theta'.$$
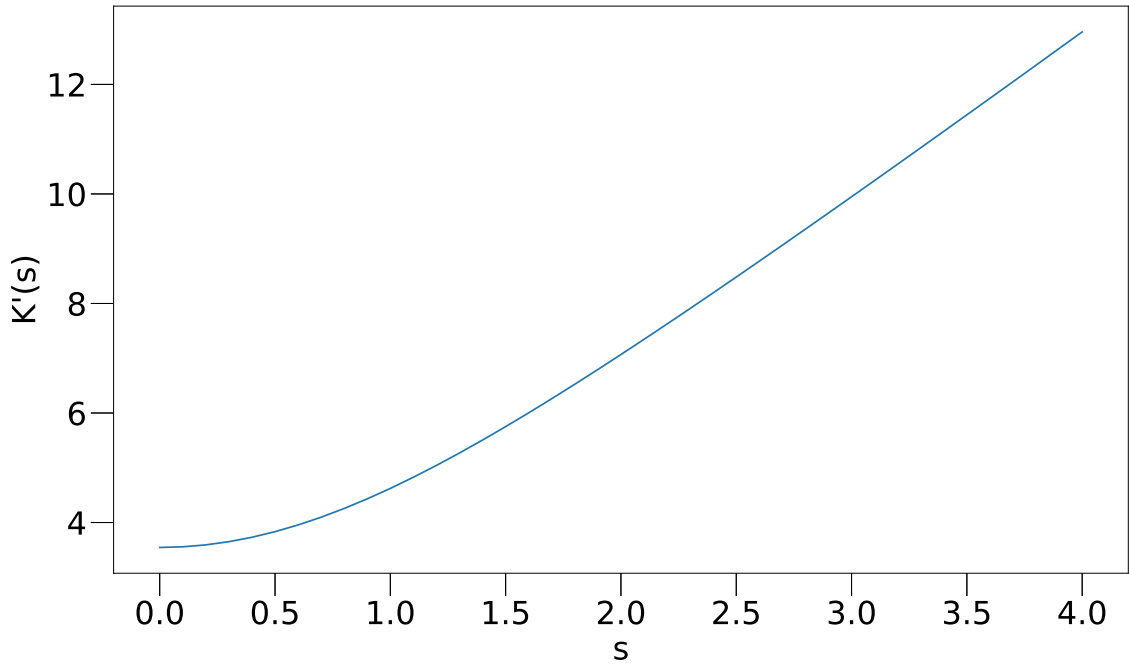
Figure A.1: Numerical result of the integral function $K'(s)$ as a function of the velocity ratio $s = v_{\mathrm{d}}/v_{\mathrm{th}}$, where v_{d} is the drift velocity and v_{th} is the thermal gas velocity.

Let $x = \frac{v}{v_{\mathrm{th}}}, s = \frac{v_{\mathrm{d}}}{v_{\mathrm{th}}}$

$$\frac{dN}{dt} = na^2 v_{\mathrm{th}} \int_0^\pi \int_0^\infty \int_0^{2\pi} \int_0^{\frac{\pi}{2}} x^3 \sin\theta \cos\theta \left(\frac{1}{\pi}\right)^{3/2} \times$$

$$e^{-(x^2 - 2xs \sin\theta \sin\theta' \cos\phi - 2xs \cos\theta \cos\theta' + s^2)} \times \qquad (A.4)$$

$$d\theta d\phi dx 2\pi \sin\theta' d\theta'.$$

We can define the integral function $K(s)$ as:

$$K'(s) = \int_0^\pi \int_0^\infty \int_0^{2\pi} \int_0^{\frac{\pi}{2}} x^3 \sin\theta \cos\theta \left(\frac{1}{\pi}\right)^{3/2} \times$$

$$e^{-(x^2 - 2xs \sin\theta \sin\theta' \cos\phi - 2xs \cos\theta \cos\theta' + s^2)} \times \qquad (A.5)$$

$$d\theta d\phi dx 2\pi \sin\theta' d\theta',$$

whose numerical result is shown in Fig.A.1 The result can be approximated as:

$$K(s) = \pi(s + e^{-s} - 1) + 2\sqrt{\pi}. \qquad (A.6)$$

80
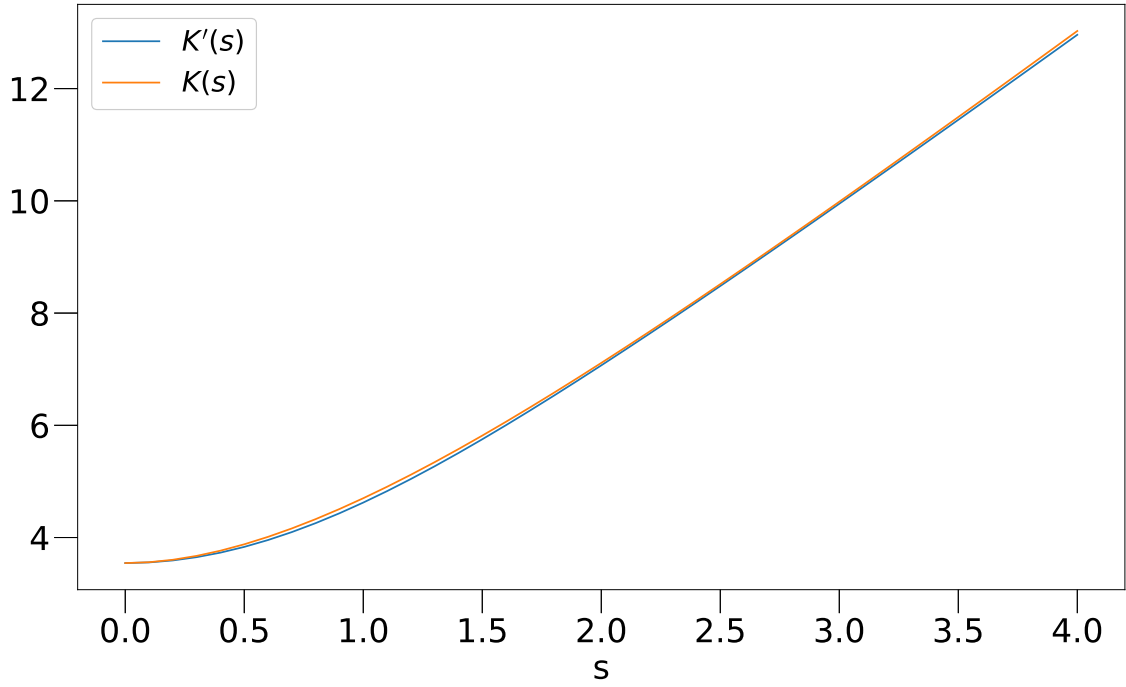
Figure A.2: Comparison of the numerical result $K'(s)$ and the approximated result $K(s)$ of the integral function as a function of the velocity ratio $s = v_{\rm d}/v_{\rm th}$, where $v_{\rm d}$ is the drift velocity and $v_{\rm th}$ is the thermal gas velocity.

Fig. A.2 illustrates the good agreement between the numerical and the approximated result.

Therefore, the damping timescale of a dust grain damped by hydrogen gas can be approximated as:

$$\tau_{\rm H} = \frac{I}{\frac{2}{3}m_{\rm H}a^2\frac{dN}{dt}} = \frac{3I}{2n_{\rm H}m_{\rm H}a^4 v_{\rm th}K(s)}. \tag{A.7}$$

In the case where $v_{\rm d} \gg v_{\rm th}$, $K(s) \approx \pi s$, we recover the result in Hoang & Lee (2019) as:

$$\tau_{\rm H}(v_{\rm d}) = \frac{3I}{2n_{\rm H}m_{\rm H}\pi a^4 v_{\rm d}}. \tag{A.8}$$

For the case where $v_{\rm d} \ll v_{\rm th}$, $K(s) \approx 2\sqrt{\pi}$, we recover the result in Hoang (2019) as:

$$\tau_{\rm H}(v_{\rm d}) = \frac{3I}{4\sqrt{\pi}n_{\rm H}m_{\rm H}a^4 v_{\rm th}}. \tag{A.9}$$

81

Appendix B — Radiation Pressure Cross-Section Efficiency in the Rayleigh Regime

The radiation pressure efficiency, as described by (Voshchinnikov, 1990), is:

$$Q_{\mathrm{pr}} = Q_{abs} + (1 - \langle \cos \Theta \rangle)Q_{sca}, \tag{B.10}$$

where Θ is the angle between the incident and scattered radiation, and $\langle \cos \Theta \rangle$ is the mean value of $\cos \Theta$. For particles in the Rayleigh regime, with size parameter $x = 2\pi a/\lambda$, the absorption efficiency is given by (Friedlander, 2000) as:

$$Q_{abs} = -4x \Im \frac{m^2 - 1}{m^2 + 2}, \tag{B.11}$$

and the scattering efficiency is:

$$Q_{sca} = \frac{8}{3} x^4 \Re \frac{m^2 - 1}{m^2 + 2}^2, \tag{B.12}$$

where m is the refractive index of the particle, which depends on the material of the particle and the wavelength of the incident radiation. Since Q_{sca} is much smaller

compared to Q_{abs}, the radiation pressure efficiency can be approximated as:

$$Q_{\text{pr}} = -4x\Im\frac{m^2-1}{m^2+2} + \frac{8}{3}x^4\Re\left(\frac{m^2-1}{m^2+1}\right)^2 (1 - \langle\cos\Theta\rangle)$$
$$\simeq -4x\Im\frac{m^2-1}{m^2+2}. \tag{B.13}$$

Equation B.13 shows that the radiation pressure efficiency in the Rayleigh regime is $Q_{\text{pr}} \propto a$. The average radiation pressure efficiency is:

$$\langle Q_{\text{pr}}\rangle = \frac{\int Q_{\text{pr}}u_\lambda d\lambda}{\int u_\lambda d\lambda}. \tag{B.14}$$

Appendix C — Effects of Interplanetary Magnetic Field on Grain Alignment and Disruption

In general, in the absence of magnetic fields, dust grains are aligned solely by radiative torques, where the angular momentum vector $\boldsymbol{J}$ aligns with the radiation direction ($\boldsymbol{k}$). This alignment mechanism is referred to as k-RAT in the context of grain alignment physics (Hoang et al., 2023). A fraction of grains, denoted by f_{highJ}, achieve alignment at high-$\boldsymbol{J}$ attractor points under this mechanism. In the presence of magnetic torques, the grain undergoes Larmor precession, causing $\boldsymbol{J}$ to align with the external magnetic field. This alignment process is termed $\boldsymbol{B}$-RAT (Hoang et al., 2023). Magnetic torques play a crucial role in aligning grains with the magnetic field, and the fraction f_{highJ} differs from that observed in k-RAT. In the presence of an electric torque, the grain will precess around the electric field $\boldsymbol{E}$, which is referred to as $\boldsymbol{E}$-RAT. The detailed discussion of these processes can be found in (Hoang et al., 2023). Below, we briefly discuss the effects of interplanetary magnetic fields on the grain rotational dynamics.

C.1 Interplanetary magnetic fields

Inside the heliosphere, the large-scale structure and dynamics of the heliospheric magnetic field are mainly shaped by the solar wind flow (Owens & Forsyth, 2013). Lazarian & Hoang (2007) demonstrated that dust grains can be trapped in high-J attractor points in the presence of a magnetic field due to the fast Larmor precession. However, if the dust grain's center of charge is offset from its center of mass, the Lorentz force exerts a torque on it. To assess the magnitude of this torque, it is essential to evaluate the strengths of both the magnetic field and the electric dipole moment.

The radial component of the magnetic field in the heliosphere can be approximated using an empirical formula derived from in situ measurements (Mann et al., 2023):

$$B_r(r) = \frac{6}{r^3}R_\odot^3 + \frac{1.18}{r^2}R_\odot^2, \tag{C.15}$$

where r is the heliocentric distance, $R_\odot$ is the radius of the Sun, and B_r is given in Gauss (G). The azimuthal component of the magnetic field in the ecliptic plane can then be determined using the Parker model (Owens & Forsyth, 2013):

$$B_\phi(r) = -B_r(r) \cdot \frac{\Omega_\odot r}{v_p}, \tag{C.16}$$

where $\Omega_\odot = 2.968 \times 10^{-6}\,\mathrm{s}^{-1}$ is the angular velocity of the Sun, and the speed of the solar wind v_p can be obtained from the following equation (Mann et al., 2023):

$$v'(r)^2 - \ln v'(r)^2 = 4 \cdot \ln r' + \frac{4}{r'} - 3, \tag{C.17}$$

with $v'(r) = v_p(r)/v_c$ (where $v_c = (kT/\tilde{\mu}m_p)^{1/2}$ is the critical velocity) and $r' = r/r_c$ (where $r_c = GM_\odot/2v_c^2$ is the critical radius). Here, k is the Boltzmann constant, $T = 8.3 \times 10^4\,\mathrm{K}$ is the temperature of the solar wind, m_p is the proton mass, G is the gravitational constant, $M_\odot$ is the mass of the Sun, and $\tilde{\mu} = 0.57$ is the mean molecular weight of the heliospheric plasma.

Therefore, the magnitude of the magnetic field B_{tot} can be expressed as:

$$
\begin{aligned}
\left| \boldsymbol{B}_{\mathrm{tot}}(r) \right| &= \left| B_r(r)\hat{\boldsymbol{r}} + B_\phi(r)\hat{\boldsymbol{\phi}} \right| \\
&= B_r(r)\sqrt{1 + \left(\frac{\Omega_\odot r}{v_p} \right)^2}.
\end{aligned}
\tag{C.18}
$$

C.2 Interaction of magnetic fields with grain magnetic dipole moment

Now, we examine the effects of interplanetary magnetic field on grain rotational dynamics, which are governed by the interaction between the magnetic field and grain electric or magnetic dipole moments.

We first discuss the interaction of magnetic fields with the grain magnetic dipole moments. When a charged dust grain rotates, a magnetic dipole moment is generated due to the motion of charges and the Barnett effect. The torque exerted by the magnetic field on the magnetic dipole causes precession around the magnetic field direction. Let us assume that a dust grain of size a rotates with an angular velocity ω. The magnitudes of the magnetic dipole moment $\left| \boldsymbol{\mu}_b \right|$ and the corresponding torque $|\Gamma_b|$ can be estimated by modeling the grain as a uniformly charged sphere

87

with charge $Q = aV$ (Weingartner, 2006):

$$
\begin{aligned}
\left|\boldsymbol{\mu}_b\right| &= \frac{1}{3}a^2 Q\omega \\
&\approx 1.1 \times 10^{-19}\left(\frac{V}{3\,\mathrm{V}}\right)\left(\frac{a}{0.1\,\mu\mathrm{m}}\right)^3\left(\frac{\omega}{10^9\,\mathrm{s}^{-1}}\right) \mathrm{dyne\,cm\,G}^{-1},
\end{aligned} \qquad (\mathrm{C}.19)
$$

$$
\begin{aligned}
\left|\boldsymbol{\Gamma}_b\right| &= \left|\boldsymbol{\mu}_b \times \boldsymbol{B}_{\mathrm{tot}}\right| \\
&= \left|\boldsymbol{\mu}_b\right| B_r(r)\sqrt{1 + \left(\frac{\Omega_\odot r}{v_{\mathrm{p}}}\right)^2}\left|\sin\phi_b\right|,
\end{aligned} \qquad (\mathrm{C}.20)
$$

where ϕ_b is the angle between the magnetic dipole vector $\boldsymbol{\mu}_b$ and the magnetic field $\boldsymbol{B}_{\mathrm{tot}}$, V is the surface potential of heliospheric dust (Horányi, 1996; Kimura & Mann, 1998), and $10^9\,\mathrm{s}^{-1}$ is the fastest spin rate of a micron-sized dust before rotational disruption (see Equation 2.28).

The magnetic dipole moment can also be generated by Barnett effect. To evaluate its magnitude, consider silicate grains with the structural unit $\mathrm{MgFeSiO_4}$ for paramagnetic dust grains, and carbonaceous grains with $\approx 10\%$ H incorporation for weakly paramagnetic dust grains. The magnitude of the magnetic dipole moments $\left|\mu_{\mathrm{Bar}}\right|$ are given by (Weingartner, 2006):

$$
\begin{aligned}
\left|\boldsymbol{\mu}_{\mathrm{Bar}}\right|(\mathrm{sil}) &\approx 1.2 \times 10^{-15}\left(\frac{T_{\mathrm{d}}}{15\,\mathrm{K}}\right)^{-1}\left(\frac{a}{0.1\,\mu\mathrm{m}}\right)^3 \\
&\quad \times \left(\frac{\omega}{10^9\,\mathrm{s}^{-1}}\right) \mathrm{dyne\,cm\,G}^{-1},
\end{aligned} \qquad (\mathrm{C}.21)
$$

for silicate grains, and

$$\left|\boldsymbol{\mu}_{\text{Bar}}\right|(\text{carb}) \approx 1.5 \times 10^{-19} \left(\frac{T_{\text{d}}}{15\,\text{K}}\right)^{-1} \left(\frac{a}{0.1\,\mu\text{m}}\right)^3$$
$$\times \left(\frac{\omega}{10^9\,\text{s}^{-1}}\right) \text{dyne cm G}^{-1}, \tag{C.22}$$

for carbonaceous grains. The magnitude of the corresponding torque $|\boldsymbol{\Gamma}_{\text{Bar}}|$ is given by:

$$\left|\boldsymbol{\Gamma}_{\text{Bar}}\right| = \left|\boldsymbol{\mu}_{\text{Bar}} \times \boldsymbol{B}_{\text{tot}}\right|$$
$$= \left|\boldsymbol{\mu}_{\text{Bar}}\right| B_r(r) \sqrt{1 + \left(\frac{\Omega_{\odot} r}{v_{\text{p}}}\right)^2} \left|\sin \phi_{\text{Bar}}\right|, \tag{C.23}$$

where ϕ_{Bar} is the angle between the magnetic dipole vector $\boldsymbol{\mu}_{\text{Bar}}$ and the magnetic field $\boldsymbol{B}_{\text{tot}}$.

Due to these magnetic torques, the grain undergoes Larmor precession, causing $\boldsymbol{J}$ to align with the external magnetic field via B-RAT (see e.g., Hoang et al. 2023).

C.3   Interaction with grain electric dipole moment

A dust grain of asymmetric charge distribution has an electric dipole moment, which can be described by $\boldsymbol{\mu}_{\text{e}} = Q \cdot \xi a \hat{\boldsymbol{x}}$, where ξa represents the displacement between the center of mass of the grain and the centroid of the charge (Draine & Lazarian, 1998), $\hat{x}$ is the unit vector pointing from the center of mass to the centroid of the charge, and $Q = aV$ represents the total charge on the grain. Here, $V = 3\,\text{V}$ is the surface potential (Kimura & Mann, 1998).

When a dust grain moves across the magnetic field, it experiences an induced

electric field, $\boldsymbol{E}_{\mathrm{ind}} = \left(\frac{\boldsymbol{v}}{c}\right) \times \boldsymbol{B}$, due to the interplanetary magnetic field (Hoang & Loeb, 2017). The torque exerted by this induced electric field on the grain's electric dipole moment ($\boldsymbol{\Gamma}_{\mathrm{ed}}$) can induce the precession of the grain angular momentum around $\boldsymbol{E}$, which can lead to the alignment of $\boldsymbol{J}$ with $\boldsymbol{E}$ by RATs, which is called E-RAT (e.g., Lazarian 2020).

The magnitude of this electric torque can be calculated as (Hoang & Loeb, 2017; Lhotka & Narita, 2019):

$$\begin{aligned}
\left|\boldsymbol{\Gamma}_{\mathrm{ed}}\right| &= \left|\boldsymbol{\mu}_e \times \boldsymbol{E}_{\mathrm{ind}}\right| \\
&\simeq \xi a^2 V \left(\sqrt{\frac{GM_\odot}{r}} - \Omega_\odot r \right) \cdot B_r(r) \left|\sin \phi_{\mathrm{ed}}\right|,
\end{aligned} \qquad \text{(C.24)}$$

where $\Omega_\odot = 2.968 \times 10^{-6}\,\mathrm{s^{-1}}$ is the angular velocity of the Sun, and ϕ_{ed} is the angle between the electric dipole vector $\boldsymbol{\mu}_e$ and the cross-product vector $\boldsymbol{v} \times \boldsymbol{B}$.

For dust grains with high angular momentum $\boldsymbol{J}$, the net electric and magnetic dipole moments, averaged over rapid spinning, are aligned with $\boldsymbol{J}$. As a result, the net torque acts perpendicular to $\boldsymbol{J}$, leaving the magnitude of the angular velocity unchanged (Hoang et al., 2023). Conversely, for dust grains with low angular momentum $\boldsymbol{J}$, the electric dipole torque can align with $\boldsymbol{J}$ and slow the grain's rotation. Assuming a dust grain with $a > \bar{\lambda}/1.8$ and $r \gg \sqrt[3]{\frac{GM_\odot}{\Omega_\odot^2}} \approx 0.17\,\mathrm{au}$, the first term in Equation C.24 becomes negligible. The heliocentric distance r_a, at which $\Gamma_{\mathrm{RAT}} = \left|\boldsymbol{\Gamma}_{\mathrm{ed}}(\phi_{\mathrm{ed}} = \pi/2)\right|$, can be derived by combining Equations 2.18 and C.24:

$$r_a \approx \frac{2.22}{\xi}\,\mathrm{au}. \qquad \text{(C.25)}$$

For $r < r_a$, $\Gamma_{\mathrm{RAT}} > \left|\boldsymbol{\Gamma}_{\mathrm{ed}}(\phi_{\mathrm{ed}} = \pi/2)\right|$, resulting in continuous spin-up of the dust grain.

Using $\xi = 0.01$ as suggested by Draine & Lazarian (1998), we find $r_a \approx 222\,\text{au}$. This calculation indicates that within the heliosphere, radiative torques consistently dominate over electric dipole torques. Consequently, for simplicity, we neglect the effects of electric torques in the discussion of RATD for the remainder of this paper.

C.4 Relative effects of magnetic to electric torques

Due to the electric torques, the grain's electric dipole moment, and consequently $\boldsymbol{J}$, can precess around the induced electric field $\boldsymbol{E}_{\text{ind}}$. This results in $\boldsymbol{J}$ aligning with $\boldsymbol{E}_{\text{ind}}$, a process known as E-RAT (Hoang et al., 2023). The fraction f_{highJ} in this scenario also differs from the fractions observed in k-RAT and B-RAT.

When both electric and magnetic torques act on a dust grain, its precession behavior depends on the relative magnitudes of the torques. If the magnetic dipole torque $\left|\boldsymbol{\Gamma}_b\right|$ or the torque induced by the Barnett effect $\left|\boldsymbol{\Gamma}_{\text{Bar}}\right|$ dominates over the electric dipole torque $\left|\boldsymbol{\Gamma}_{\text{ed}}\right|$, the grain precesses around the magnetic field $\boldsymbol{B}$. Conversely, if the electric dipole torque is dominant, precession occurs around the induced electric field $\boldsymbol{E}_{\text{ind}}$. For clarity, let $\left|\boldsymbol{\Gamma}_{\text{ed,max}}\right|$, $\left|\boldsymbol{\Gamma}_{b,\text{max}}\right|$, and $\left|\boldsymbol{\Gamma}_{\text{Bar,max}}\right|$ represent the maximum torques corresponding to $\phi_{\text{ed}} = \pi/2$, $\phi_b = \pi/2$, and $\phi_{\text{Bar}} = \pi/2$, respectively.

To better understand the relative importance of magnetic, electric, and radiative torques on grain alignment, we need to compare the characteristic timescales of precession induced by these torques, as in e.g., Hoang et al. (2023). Here we compare their relative magnitudes for convenience. The ratio of magnitude between the electric dipole torque, $\left|\boldsymbol{\Gamma}_{\text{ed,max}}\right|$, and the magnetic dipole torque, $\left|\boldsymbol{\Gamma}_{b,\text{max}}\right|$. This ratio

91

can be derived by combining Equations C.24 and C.20:

$$
\frac{\left|\boldsymbol{\Gamma}_{\text{ed,max}}\right|}{\left|\boldsymbol{\Gamma}_{b,\text{max}}\right|} \approx \frac{3\xi\Omega_{\odot}r}{\omega a}\left(1+\left(\frac{\Omega_{\odot}r}{v_{\text{p}}}\right)^{2}\right)^{-\frac{1}{2}}
$$

$$
\approx 133\left(\frac{a}{0.1\,\mu\text{m}}\right)^{-1}\left(\frac{\omega}{10^{9}\,\text{s}^{-1}}\right)^{-1}\left(\frac{r}{1\,\text{au}}\right)
$$

$$
\times\left(1+\left(\frac{\Omega_{\odot}r}{v_{\text{p}}}\right)^{2}\right)^{-\frac{1}{2}}. \tag{C.26}
$$

For a dust grain trapped at high-J attractor points, the fastest spin rate is determined by the critical rotational velocity $\omega = \omega_{\text{disr}}$ (see Equation 2.28). By combining Equations 2.28 and C.20, we derive:

$$
\frac{\left|\boldsymbol{\Gamma}_{\text{ed,max}}\right|}{\left|\boldsymbol{\Gamma}_{b,\text{max}}\right|} \approx 37\hat{\rho}^{1/2}S_{\text{max},9}^{-1/2}\left(\frac{r}{1\,\text{au}}\right)\left(1+\left(\frac{\Omega_{\odot}r}{v_{\text{p}}}\right)^{2}\right)^{-\frac{1}{2}}. \tag{C.27}
$$

Conversely, for a dust grain trapped at low-J attractor points, the angular velocity can be approximated as the thermal angular velocity, $\omega_{\text{th}} = \sqrt{2kT_{\text{gas}}/I}$ (Hoang & Lazarian, 2014). In this case, the ratio becomes:

$$
\frac{\left|\boldsymbol{\Gamma}_{\text{ed,max}}\right|}{\left|\boldsymbol{\Gamma}_{b,\text{max}}\right|} \approx 5.7\times10^{5}\hat{\rho}^{1/2}\left(\frac{a}{0.1\,\mu\text{m}}\right)^{1.5}\left(\frac{T}{100\,\text{K}}\right)^{-1}\left(\frac{r}{1\,\text{au}}\right)
$$

$$
\times\left(1+\left(\frac{\Omega_{\odot}r}{v_{\text{p}}}\right)^{2}\right)^{-\frac{1}{2}}. \tag{C.28}
$$

Similarly, the ratio between the magnetic dipole torque, $\left|\boldsymbol{\Gamma}_{b,\text{max}}\right|$, and the torque induced by the Barnett effect, $\left|\boldsymbol{\Gamma}_{\text{Bar,max}}\right|$, can be derived from Equations C.20 and

C.23:

$$\frac{\left|\mathbf{\Gamma}_{b,\max}\right|}{\left|\mathbf{\Gamma}_{\mathrm{Bar,max}}\right|} \approx \frac{\left|\boldsymbol{\mu}_b\right|}{\left|\boldsymbol{\mu}_{\mathrm{Bar}}\right|}$$

$$\approx \begin{cases} 9.4 \times 10^{-5} \left(\frac{V}{3\,\mathrm{V}}\right)\left(\frac{T_\mathrm{d}}{15\,\mathrm{K}}\right) & \text{(silicate)}, \\[2mm] 0.74 \left(\frac{V}{3\,\mathrm{V}}\right)\left(\frac{T_\mathrm{d}}{15\,\mathrm{K}}\right) & \text{(carbonaceous)}. \end{cases} \tag{C.29}$$

Equations C.27, C.28, and C.29 suggest that, for paramagnetic grains at high-J attractor points, the magnetic dipole moment generated by the Barnett effect typically dominates, making B-RAT the prevailing alignment mechanism. In contrast, for weakly paramagnetic grains at high-J attractor points, and for grains at low-J attractor points, the electric dipole torque can surpass both the magnetic dipole and the torque induced by the Barnett effect, leading to E-RAT as the dominant alignment mechanism.

C.5 k-RAT and relative effects of radiative to electric torques

Lazarian & Hoang (2007) demonstrated that the third component of RAT ($\Gamma_{\mathrm{RAT,e3}}$) induces grain precession around the radiation direction ($\boldsymbol{k}$). When the radiative precession timescale is shorter than the damping timescale, the radiation direction becomes the axis of grain alignment. This alignment mechanism is referred to as k-RAT Hoang et al. 2023.

In the heliosphere, while the averaging RAT efficiency for spin up the dust grains is approximately $\langle Q_\Gamma \rangle \approx 0.4$ for $a > \bar{\lambda}/1.8$ (see Equation 2.17), the third component of the RAT efficiency for grain precession has much smaller value $Q_{\Gamma,\mathrm{e3}} \approx 0.01$ (Hoang

& Lazarian, 2014). Therefore, the third component of the torque $\Gamma_{\text{RAT,e3}}$ can be expressed as:

$$\Gamma_{\text{RAT,e3}} = 2.16 \times 10^{-29} a_{-5}^2 \gamma_{\text{rad}} U \bar{\lambda}_{0.5} \left(\frac{Q_{e3}}{0.01}\right) \text{dyne cm}$$

$$= 2.1 \times 10^{-21} a_{-5}^2 \left(\frac{r}{1\,\text{au}}\right)^{-2} \left(\frac{Q_{e3}}{0.01}\right) \text{dyne cm}, \tag{C.30}$$

where $a_{-5} = a/10^{-5}\,\text{cm}$, $\bar{\lambda}_{0.5} = \bar{\lambda}/0.5\,\mu\text{m}$, and Q_{e3} is the third component of RAT efficiency (Hoang & Lazarian, 2014).

The ratio between the third component of RAT torque and the electric dipole torque can be derived by combining Equations C.24 and C.30:

$$\frac{\Gamma_{\text{RAT,e3}}}{|\mathbf{\Gamma}_{\text{ed,max}}|} \approx 15 \left(\frac{V}{3\,\text{V}}\right)^{-1} \left(\frac{r}{1\,\text{au}}\right)^{-3} \left(\frac{10^{-5}\,\text{G}}{B_r}\right) \left(\frac{Q_{e3}}{0.01}\right). \tag{C.31}$$

Assuming $Q_{e3} = 0.01$ and referring to the conclusions in Section C.4, Equation C.31 suggests that for weakly paramagnetic grains at high-J attractor points, as well as for grains at low-J attractor points, k-RAT dominates over E-RAT at heliocentric distances $r < 5\,\text{au}$.

94